LUND UNIVERSITY

# Big Lessons from Small Bacteria

## Following Photo-driven Processes in Photosynthetic Systems with Multidimensional Spectroscopy

Bukarte, Egle

2023

*Document Version:*
Publisher's PDF, also known as Version of record

Link to publication

*Citation for published version (APA):*
Bukarte, E. (2023). *Big Lessons from Small Bacteria: Following Photo-driven Processes in Photosynthetic Systems with Multidimensional Spectroscopy* (1 ed.). Lund University.

*Total number of authors:*
1

LUND UNIVERSITY

PO Box 117
221 00 Lund
+46 46-222 00 00

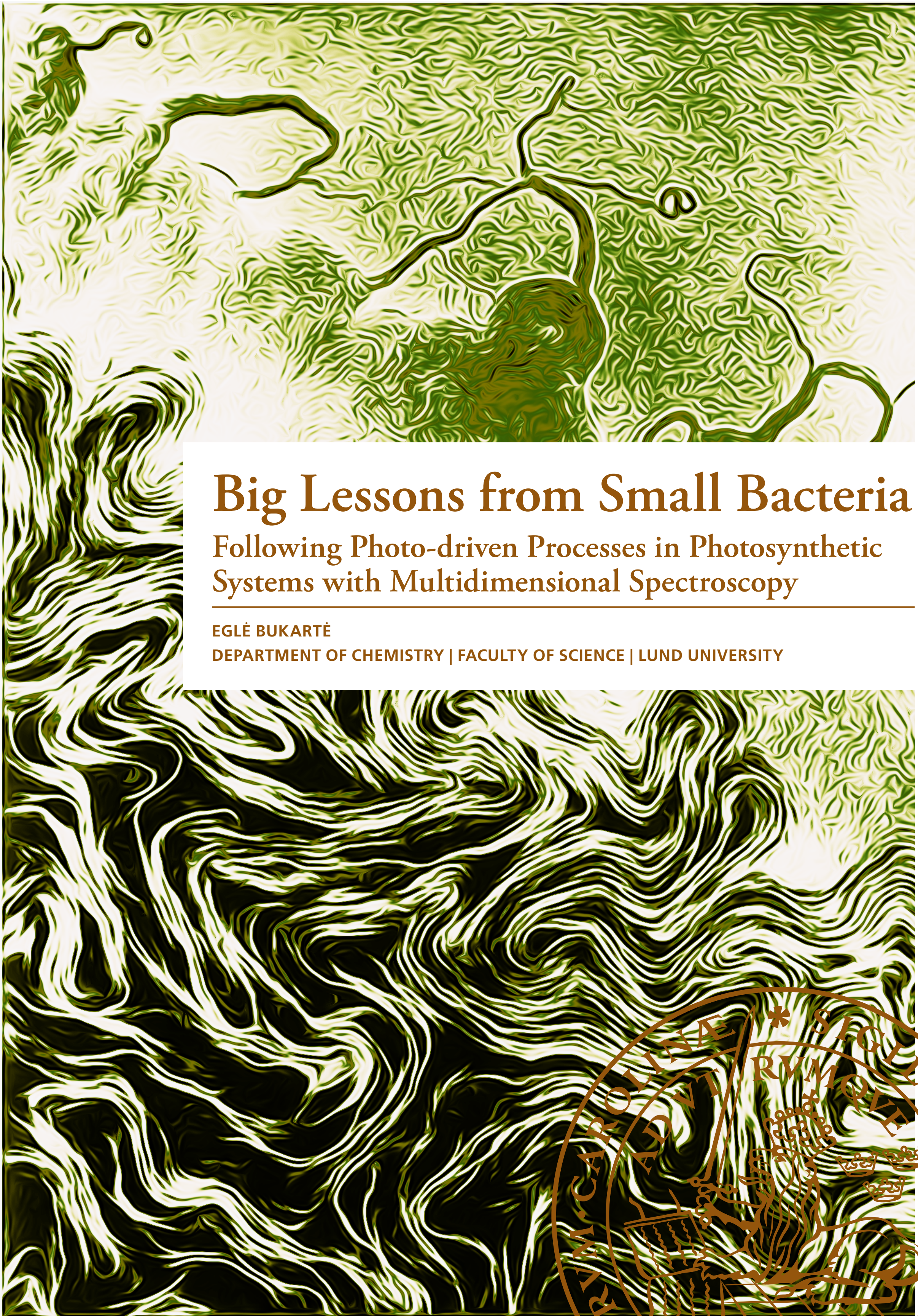

# Big Lessons from Small Bacteria

## Following Photo-driven Processes in Photosynthetic Systems with Multidimensional Spectroscopy

EGLĖ BUKARTĖ

DEPARTMENT OF CHEMISTRY | FACULTY OF SCIENCE | LUND UNIVERSITY

# Big Lessons from Small Bacteria

# Big Lessons from Small Bacteria

## Following Photo-driven Processes in Photosynthetic Systems with Multidimensional Spectroscopy

Eglė Bukartė

LUND UNIVERSITY

DOCTORAL DISSERTATION

Doctoral dissertation for the degree of Doctor of Philosophy (PhD) at the Faculty of Science at Lund University to be publicly defended on the 31st of March 2023 at 09.15 in Kemicentrum Lecture hall C, Department of Chemistry, Naturvetarvägen 14, 22100 Lund

*Faculty opponent*
Professor Herbert van Amerongen,
Department of Physics, Wageningen University

**Organization**
LUND UNIVERSITY

Division of Chemical Physics
Department of Chemistry
P.O. Box 124, SE-22100 Lund, Sweden

**Author**
Eglė Bukartė

**Document name**
Doctoral dissertation

**Date of issue**
2023-03-06

Sponsoring organization

**Title and subtitle**
Big Lessons from Small Bacteria:
Following Photo-driven Processes in Photosynthetic Systems with Multidimensional Spectroscopy

**Abstract**

Sunlight is a plentiful, continuously flowing source of energy, fuelling life on Earth as we know it. To use this potential, plants, cyanobacteria and photosynthetic bacteria evolved to absorb solar radiance and convert it into a chemically stable form by performing a process known as *photosynthesis*. Despite a wide variety of photosynthetic systems, the initial steps of photosynthesis are similar. They involve the absorption of photons by light-harvesting antennas, transferring this energy to photosynthetic reaction centres and primary charge separation.

Over the recent decades, scientists put much effort into understanding the driving forces behind the photosynthetic processes. Exploring bacterial photosynthesis became a field of its own due to their high robustness towards living conditions and efficient energy transfer and trapping within photosynthetic units. However, sizes in the nanometre scale, high pigment densities and congested absorption spectra, energy and electron transfer rates from hundreds of femtoseconds to tens of picoseconds made the primary steps of bacterial photosynthesis challenging to follow and explore.

This thesis presents studies of photo-driven processes inside various photosynthetic systems using two-dimensional electronic spectroscopy, an advanced technique combining high temporal and spectral resolutions and well suited for studying excitation-induced processes within photo-active systems. The first chapter of this thesis introduces the main photosynthetic systems under investigation: chlorophyll-type molecules, bacterial reaction centres and photosynthetic units of the purple bacterium *Rhodobacter sphaeroides* and the green bacterium *Chloroflexus aurantiacus*. The second chapter delivers a detailed introduction to the main experimental technique – two-dimensional electronic spectroscopy – and provides background on following and understanding recorded signals.

The results chapter of this thesis summarises observations of vibronic coupling inside chlorophyll *c1* molecule. In addition, it presents energy and electron transfer dynamics within the bacterial reaction centres from the purple bacterium *Rhodobacter sphaeroides* and the green bacterium *Chloroflexus aurantiacus* and describes means to identify precursor states for charge transfer in (most probably every) reaction centre. Final results present mapping excitation energy transfer and trapping processes inside intact living cells of the green bacterium *Chloroflexus aurantiacus.* The thesis finishes with concluding remarks and some future directions.

**Key words** Two-dimensional electronic spectroscopy, Ultrafast spectroscopy, Chlorophyll, Bacterial reaction centers, Photosynthetic unit, Purple bacteria, Green bacteria

Classification system and/or index terms (if any)

Supplementary bibliographical information

**Language** English

**ISSN** and key title

**ISBN**
The printed version: 978-91-7422-932-5
The digital version: 978-91-7422-933-2

Recipient's notes

**Number of pages** 74

Price

Security classification

Signature

Date 2023-02-20

# Big Lessons from Small Bacteria

## Following Photo-driven Processes in Photosynthetic Systems with Multidimensional Spectroscopy

Eglė Bukartė

LUND
UNIVERSITY

Cover photo adapted from Pierson, B.K.; Castenholz, R.W. A phototrophic gliding filamentous bacterium of hot springs, *Chloroflexus aurantiacus*, gen. and sp. nov. *Arch. Microbiol*., **1974** 100 (1), 5–24, in agreement with Springer Nature under the License Number 5461830820940.

Faculty of Science
Department of Chemistry

ISBN
The printed version: 978-91-7422-932-5
The digital version: 978-91-7422-933-2

Printed in Sweden by Media-Tryck, Lund University
Lund 2023

Printed matter
3041 0903

Media-Tryck is a Nordic Swan Ecolabel
certified provider of printed material.
Read more about our environmental
work at www.mediatryck.lu.se

MADE IN SWEDEN

*To my husband and our two beautiful boys*

# Table of Contents

Abstract ........................................................................................10
Popular Scientific Summary.......................................................................11
List of Papers......................................................................................13
Author's contribution to the papers...........................................................14
Abbreviations ....................................................................................15

**Introduction ......................................................................................17**
Outline of this thesis............................................................................19

**Bacterial photosynthesis ...................................................................21**
A pigment as a photosynthetic building unit...............................................21
Bacteria under the scope of this work .......................................................23
  The purple bacterium *Rhodobacter sphaeroides*...............................23
  The green bacterium *Chloroflexus aurantiacus* ................................25
  Bacterial reaction centres..................................................................26

**Two-dimensional electronic spectroscopy .........................................31**
2DES – a long story short .....................................................................31
The brief theory behind the response function formalism...........................33
  Hamiltonian of a system ....................................................................33
  Third-order response function .............................................................35
Tracking 2DES signals..........................................................................36
  Conventional double-sided Feynman diagrams.......................................36
  Constructing a two-dimensional spectrum ............................................38
  2D spectra for various systems: introducing re-excitation pathways ..40
Experimental nuances ..........................................................................43
  Experimental setup ...........................................................................43
  Polarisation control............................................................................45
  Global analysis procedure ..................................................................47

**Main results.......................................................................................51**
Vibronic coupling in chlorophyll-type molecules........................................51
Dynamic band-shift signal in bRC ...........................................................53
2DES of bacterial reaction centres ..........................................................56

Low temperature absorption spectra....................................................56
Excitation energy and electron transfer timescales ..............................58
Identification of charge transfer states..................................................59

Energy flow and trapping in the living cells of *Cfx. Aurantiacus*................61

**Concluding remarks.................................................................................64**

**The outlook..............................................................................................65**

**References ...............................................................................................66**

# Abstract

Sunlight is a plentiful, continuously flowing source of energy, fuelling life on Earth as we know it. To use this potential, plants, cyanobacteria and photosynthetic bacteria evolved to absorb solar radiance and convert it into a chemically stable form by performing a process known as *photosynthesis*. Despite a wide variety of photosynthetic systems, the initial steps of photosynthesis are similar. They involve the absorption of photons by light-harvesting antennas, transferring this energy to photosynthetic reaction centres and primary charge separation.

Over the recent decades, scientists put much effort into understanding the driving forces behind the photosynthetic processes. Exploring bacterial photosynthesis became a field of its own due to their high robustness towards living conditions and efficient energy transfer and trapping within photosynthetic units. However, sizes in the nanometre scale, high pigment densities and congested absorption spectra, energy and electron transfer rates from hundreds of femtoseconds to tens of picoseconds made the primary steps of bacterial photosynthesis challenging to follow and explore.

This thesis presents studies of photo-driven processes inside various photosynthetic systems using two-dimensional electronic spectroscopy, an advanced technique combining high temporal and spectral resolutions and well suited for studying excitation-induced processes within photo-active systems. The first chapter of this thesis introduces the main photosynthetic systems under investigation: chlorophyll-type molecules, bacterial reaction centres and photosynthetic units of the purple bacterium *Rhodobacter sphaeroides* and the green bacterium *Chloroflexus aurantiacus*. The second chapter delivers a detailed introduction to the main experimental technique – two-dimensional electronic spectroscopy – and provides background on following and understanding recorded signals.

The results chapter of this thesis summarises observations of vibronic coupling inside chlorophyll *c1* molecule. In addition, it presents energy and electron transfer dynamics within the bacterial reaction centres from the purple bacterium *Rhodobacter sphaeroides* and the green bacterium *Chloroflexus aurantiacus* and describes means to identify precursor states for charge transfer in (most probably every) reaction centre. Final results present mapping excitation energy transfer and trapping processes inside intact living cells of the green bacterium *Chloroflexus aurantiacus*. The thesis finishes with concluding remarks and some future directions.

# Popular Scientific Summary

Through billions of years of evolution, nature has found a solution for efficiently harvesting sunlight – photosynthesis. The process that not only generates the oxygen that many living organisms breathe but also produces food, energy beyond photosynthesis and many materials we depend upon today. It takes an overall of ten minutes from the moment a photon is released from the Sun to be captured and its energy stored in a stable form that can persist for many years.

Photosynthesis has four phases: (1) light harvesting and energy delivery in antenna complexes, (2) charge separation and electron transfer by reaction centres, (3) energy stabilisation in the form of chemical compounds, and (4) utilisation of stabilised energy in biochemical processes. The first two steps are rapid and happen in less than a nanosecond. Their main goal is to efficiently create the spatially separated positive and negative charges and avoid recombination and losing this energy to heat and dissipation. An excellent example of efficient and, at the same time, extremely resistant photosynthesis can be found in *photosynthetic bacteria*.

To effectively collect and utilise solar energy, photosynthetic bacteria are equipped with photosynthetic units consisting of various antenna complexes and bacterial reaction centres. The light-harvesting systems have an enormous structural diversity, depending on the bacteria under study. For example, a photosynthetic unit may contain light-harvesting complexes in the shape of neat circles placed side by side next to one another. Other bacteria can grow themselves a bulky chlorosome, collecting tens of thousands of bacteriochlorophylls, clumped together and arranged in complex structures with many layers. For an efficient and unidirectional energy transfer, a photosynthetic unit may also be equipped with some mediator complexes such as baseplate, Fenna–Matthews–Olson and others. However, in every case, energy needs to end up in the bacterial reaction centre for charge separation.

The major challenge when investigating photosynthetic systems is the need for a sophisticated experimental technique to follow extremely rapid primary steps triggered by the absorption of a photon. One such method is two-dimensional electronic spectroscopy. It is a state-of-the-art technique that uses ultrashort laser pulses to measure photo-driven processes with a femtosecond time resolution. During the experiment, two laser pulses excite the system, and the system's status is 'read' with the third laser pulse. The method allows the observer to follow excitation dynamics from the very first moments after photon absorption until the relaxation of molecules to the initial state by changing the time delays between the excitation and detection pulses. It also provides knowledge about energy states and couplings, excitation energy transfer and charge separation processes, coherent energy motion and even, to some extent, the structure of the system under investigation. Since the first experiments, two-dimensional electronic spectroscopy was broadly used to study photosynthetic molecules, aggregates and recently – even intact photosynthetic bacteria.

The work of this thesis covers the studies of two primary steps of photosynthesis in photosynthetic bacteria – excitation energy transfer and charge separation – using two-dimensional electronic spectroscopy. It starts by exploring the interactions within the smallest unit of the photosynthetic system – the chlorophyll *c1* molecule. The beating signals revealed with polarisation-controlled experiments provided evidence of a complex interplay between two excited states of the system, a phenomenon known as *vibronic coupling*. After that, the focus of the thesis shifts towards the bacterial reaction centres from two different bacteria: purple bacterium *Rhodobacter sphaeroides* and green bacterium *Chloroflexus aurantiacus*. The photo-induced dynamics in both complexes were tracked up to one nanosecond after excitation, and characteristic energy transfer and charge separation rates were obtained. The most remarkable and joyful discovery from these experiments was observing initial charge transfer states in both reaction centres, a feature extensively debated within the scientific community. Lastly, the most exceptional work of this thesis is a study of excitation energy transfer and trapping within the intact living cells of the green bacterium *Chloroflexus aurantiacus*.

# List of Papers

*Paper I*

Bukartė E., Haufe A., Paleček D., Büchel C. and Zigmantas D. Revealing vibronic coupling in chlorophyll *c1* by polarization-controlled 2D electronic spectroscopy, *Chemical Physics,* **2020**, 530, 110643.

*Paper II*

Bukartė E., Paleček D., Edlund P., Westenhoff S. and Zigmantas D. Dynamic band-shift signal in two-dimensional electronic spectroscopy: A case of bacterial reaction center, *The Journal of Chemical Physics,* **2021**, 154, 115102.

*Paper III*

Bukartė E., Paleček D., Edlund P., Westenhoff S. and Zigmantas D. Revealing the precursor state to charge separation in bacterial reaction centers, *Manuscript.*

*Paper IV*

Bukartė E., Kolesnichenko P., Bina D. and Zigmantas D. Resolving multistage charge separation in *Chloroflexus aurantiacus* bacterial reaction centres, *Manuscript.*

*Paper V*

Bukartė E., Rouxel R., Bina D. and Zigmantas D., Characterizing energy transfer and trapping in living cells of photosynthetic bacteria *Chloroflexus aurantiacus*, *Manuscript.*

Publications not included in this thesis

*Paper VI*

Thyrhaug E., Schröter M., Bukartė E., Kühn O., Cogdell R., Hauer J. and Zigmantas D. Intraband dynamics and exciton trapping in the LH2 complex of Rhodopseudomonas acidophila, *The Journal of Chemical Physics,* **2021**, 154, 045102.

*Paper VII*

Butkus V., Alster J., Bašinskaitė E., Augulis R., Neuhaus P., Valkunas L. Anderson H.L., Abramavicius D. and Zigmantas, D. Discrimination of Diverse Coherences Allows Identification of Electronic Transitions of a Molecular Nanoring, *The Journal of Physical Chemistry Letters,* **2017**, 8, 2344.

# Author’s contribution to the papers

*Paper I*

I participated in the low temperature two-dimensional electronic spectroscopy experiments of chlorophyll *c1*, took part in data analysis and discussions and wrote the initial manuscript.

*Paper II*

I was involved in data analysis of *Rhodobacter sphaeroides* bacterial reaction centres data, participated in the discussions and wrote the initial manuscript.

*Paper III*

I participated in the low temperature two-dimensional electronic spectroscopy experiments of *Chloroflexus aurantiacus* bacterial reaction centres, analysed the measured data, took part in analysing *Rhodobacter sphaeroides* bacterial reaction centres data, participated in the discussions and wrote the initial manuscript.

*Paper IV*

I participated in the low temperature two-dimensional electronic spectroscopy experiments of *Chloroflexus aurantiacus* bacterial reaction centres, analysed the data, participated in the discussions and wrote the initial manuscript.

*Paper V*

I took part in the room temperature two-dimensional electronic spectroscopy experiments of *Chloroflexus aurantiacus* living cells, analysed the data, participated in the discussions and wrote the initial manuscript.

# Abbreviations

| | |
|---|---|
| 2DES | Two-dimensional electronic spectroscopy |
| AP | All-parallel |
| BChl | Bacteriochlorophyll |
| BPheo | Bacteriopheophytin |
| bRC | Bacterial reaction centre |
| $bRC_{cfx}$ | bRC from green bacterium *Chloroflexus aurantiacus* |
| $bRC_{sph}$ | bRC from purple bacterium *Rhodobacter sphaeroides* |
| Chl | Chlorophyll |
| CP | Cross-peak |
| CT | Charge-transfer |
| DAS | Decay associated spectrum |
| DC | Double-crossed |
| EET | Excitation energy transfer |
| ESA | Excited state absorption |
| ET | Electron transfer |
| FT | Fourier transform |
| GSB | Ground state bleaching |
| MA | Magic angle |
| NOPA | Non-collinear optical parametric amplifier |
| OM | Oscillation map |
| PE | Photon echo |
| PSU | Photosynthetic unit |
| RE | Re-excitation |
| SE | Stimulated emission |
| TA | Transient absorption |
| TFWM | Transient four-wave mixing |

# Introduction

Planet Earth would be a cold and desolate place if not for the process that provides oxygen and energy for the most of living organisms – photosynthesis. Photosynthesis is a process through which light energy is converted into chemical energy by plants, algae, and photosynthetic bacteria.[1] It can be divided into two branches: oxygenic photosynthesis, which happens in the presence of air,[2] and its opposite – anoxygenic photosynthesis.[3] Oxygenic photosynthesis, involving the reduction of carbon dioxide and oxidation of water to produce oxygen, is performed by higher plants, algae and cyanobacteria. Photosynthetic bacteria, such as purple or green bacteria, on the other hand, are well-known performers of anoxygenic photosynthesis, oxidising molecules other than water. Yet, regardless of the oxidisable compounds, the primary steps in both branches are similar. They cover the absorption of solar radiance by the light-harvesting antennas and excitation energy transfer through various complexes to photosynthetic reaction centres, followed by charge separation and electron transfer events for further energy trapping into a stable form of chemical bonds.[4–6]

Bacterial photosynthesis alone is a fascinating yet challenging field of studies. There are four known phylogenetic groups of anoxygenic phototrophs: the purple bacteria, the green sulphur bacteria, the green non-sulphur bacteria and the heliobacteria.[7] These photosynthetic organisms are highly robust towards living conditions. For example, purple bacteria can inhabit extreme environments, including temperatures between 0 – 57 ºC, pH values from 3 to 11 and salinities up to (~32 %), coping inside saturated NaCl solutions.[8] And these are not even the absolute survival limits of anoxygenic bacteria, as the green non-sulphur bacterium *Chloroflexus aurantiacus*, which contains a purple bacterial-type photosynthetic reaction centre,[7] can thrive at temperatures up to 70 °C.[9] Also, the first steps of photosynthesis in bacteria are known to be rather efficient. For example, the quantum yield of charge separation in photosynthetic purple and green bacteria was measured to be close to unity.[10,11] This property alone drove a great number of spectroscopic studies, all trying to define the key factors for this high quantum efficiency.[4,12,13]

For effective light capture and charge separation, photosynthetic bacteria are equipped with tens of photosynthetic units (PSUs) consisting of various antenna aggregates and bacterial reaction centres (bRCs).[14–17] Depending on the bacteria under the study, its PSU may contain light-harvesting complexes composed of tens of bacteriochlorophylls neatly arranged in a circular manner (e.g. purple bacteria

*Rhodobacter sphaeroides, Rhodoblastus acidophilus*).[18] In other bacteria, antennas can take the shape of flat elongated sacs, with round ends (chlorosomes), filled with thousands of bacteriochlorophylls, all sticking and arranging in complicated rod-/lamellar-like structures (*Chloroflexus aurantiacus, Chlorobaculum tepidum*).[19] After initial absorption, the captured energy flows through intermediate aggregates, like baseplate, Fenna–Matthews–Olson complex, B808–866 complex and others.[14–16] This great diversity of light-harvesting pigment-protein systems in PSUs from various photosynthetic bacteria exists due to their wide habitat distribution, where a single light-harvesting apparatus seems unlikely to operate robustly and efficiently.

After travelling through the light-harvesting complexes, the excitation energy is delivered to bRCs for charge separation. The bRCs are pigment-protein complexes bound to the membranes, converting absorbed/received energy into a stable transmembrane electrochemical potential through a sequence of electron-transfer steps. Photosynthetic reaction centres are separated into two groups, depending on the main electron acceptors. Type I, with iron sulphur clusters as electron acceptors, and type II, with a pair of quinones as acceptors.[1] Despite minor differences, a remarkable property of the reaction centres is their near-unity quantum yield for electron transfer, which results in approximately 40% of the energy of the input photons being stored in the transmembrane charge separation.[4,10,11,20]

Initial light capture and energy transfer raise significant challenges on their own, as the absorbed energy must be delivered to the reaction centres for charge separation faster than the main photosynthetic pigments (chlorophylls and bacteriochlorophylls) lose it through fluorescence (3–6 ns).[21] For this reason, most of the pigments in PSU are bound to the proteins or face some pigment-pigment interactions, changing their electronic behaviour and controlling the overall photo-activity of the system. This is a crucial property in order to perform an efficient energy transfer and trapping since excitations flow through the PSU on timescales of tens/hundreds of picoseconds, surpassing energy dissipation and charge recombination processes.[13,22]

This thesis focuses mainly on exploring the first two primary steps of bacterial photosynthesis – excitation energy transfer and primary charge separation. Since these processes are extremely fast, an ultrafast time-resolved technique – two-dimensional electronic spectroscopy (2DES) – was used to study them. The method provides information on the system's evolution with high time (10–20 fs) and spectral resolutions and is highly suitable for studying photo-induced processes in photo-active systems.

# Outline of this thesis

The thesis begins with an introductory chapter to the main photosynthetic systems examined in this work: chlorophyll-type molecules, PSUs of purple bacteria *Rhodobacter sphaeroides* and green bacteria *Chloroflexus aurantiacus* and their reaction centres. The second rather broad chapter overviews the main experimental technique used for studying these systems – two-dimensional electronic spectroscopy (2DES). The relative subchapters cover a small part of the third-order response function formalism, ways to follow various recorded signals and other experimental insights.

The results of this thesis are based on five research papers. Paper I examines the complex interaction – *a vibronic coupling* – between two excited states in chlorophyll *c1* molecule. Papers II, III and IV focus on the processes happening in the bRCs from purple bacteria *Rhodobacter sphaeroides* ($\mathrm{bRC_{sph}}$) and green bacteria *Chloroflexus aurantiacus* ($\mathrm{bRC_{cfx}}$). Lastly, paper V explores excitation energy transfer and trapping inside the PSU of the living intact cells of the green bacterium *Chloroflexus aurantiacus*.

The thesis concludes with finishing remarks about the findings and their impact on bacterial photosynthesis. Final comments suggest some perspectives (and hopes) for future studies.

# Bacterial photosynthesis

The first chapter of this thesis presents the main investigated photosynthetic systems. It begins with an introduction of the key pigment group – chlorophyll-type molecules – responsible for light absorption, excitation energy transfer and charge separation during the solar energy utilisation process.[20] Then the focus shifts towards this work's two main photosynthetic bacteria: the purple bacterium *Rhodobacter sphaeroides* and the green bacterium *Chloroflexus aurantiacus*. After an overview of their photosynthetic units (PSUs), the chapter introduces their principal pigment-protein complexes – the bacterial reaction centres ($bRC_{sph}$ and $bRC_{cfx}$). It should be clarified that in this work, the 2DES measurements were performed for both $bRC_{sph}$ and $bRC_{cfx}$, but only one intact PSU of *Chloroflexus aurantiacus* bacteria was examined. Yet the structures and photo-induced dynamics in PSUs from both photosynthetic bacteria are presented for consistency.

## A pigment as a photosynthetic building unit

Photosynthetic pigments, such as chlorophylls (Chls), bacteriochlorophylls (BChls), and carotenoids, are the key molecules for energy capture and transfer in photosynthetic organisms.[20] Naturally, much effort has been devoted to understanding their driving mechanisms. Electronic excitations and dynamics in Chl-type molecules with macro rings are usually described by the model developed by M. Gouterman in 1960.[23] Originally applied for porphyrins, the well-known model describes the two main electronic transitions as separate excitations, denoted as $Q_y$ and $Q_x$ ($Q_x$ being the higher energy state), with two transition dipole moments almost at a right angle to each other.[23] The transitions got their names for almost precisely matching the *x*- and *y*- molecular axes of the porphyrin ring (see Fig. 1),[20,23] but in reality, minor angle deviations are present for each photosynthetic pigment.[24]

A recent comprehensive study of various Chl-type molecules has shown that $Q_y$ and $Q_x$ transitions are not entirely separate.[25] A *vibronic coupling* between the two states must be considered to describe the photo-physical properties and excitation dynamics correctly. The vibronic coupling term, as used in this thesis, is an interaction between the higher purely electronic transition ($Q_x$) and the vibronic transitions of the lower electronic energy state ($Q_y$ + vibrational quanta), as illustrated with the energy scheme on the right side of Fig. 1. This type of interaction mixes the characters of two states – depending on their proximity to each other and the coupling strength – and alters transition energies as well as orientations and strengths of transition dipole moments.[25,26] In addition, vibronic coupling in molecular dimers and bigger aggregates is thought to contribute to efficient and swift excitation energy transfer.[26,27]

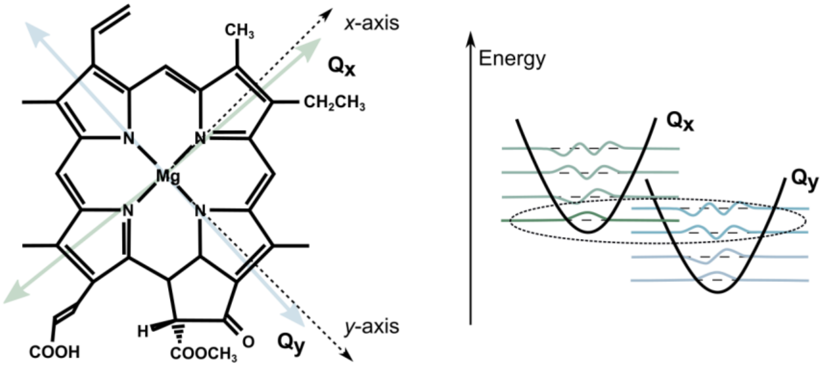

**Figure 1. Structure of Chl *c1* and vibronic coupling energy scheme**
The structure of Chl *c1,* as in ref. [28]. The molecular *x*- and *y*-axes were drawn according to ref. [20]. Two electronic $Q_y$ and $Q_x$ transitions are marked with coloured arrows. On the right is the schematic representation of two electronic states as harmonic potentials, with the lowest level of electronic origin and the higher states of vibronic (excited state vibrational) origin. The $Q_x$'s electronic transition and $Q_y$'s vibronic levels that could couple vibronically are marked by a dashed oval.

Although there is little doubt about the presence of vibronic coupling in Chl-type molecules, it is challenging to observe it experimentally. The technical difficulties rising are: (i) the significant energy difference between two electronic $Q_y$ and $Q_x$ transitions, making it difficult to excite their superposition with the same laser pulse; (ii) weak $Q_x$ transition resulting in negligible signals; and (iii) minor signals being washed away by the dominant signals from the electronic/ vibrational transitions.

The first attempt to probe vibronic coupling in Chl-type molecule with 2DES was made for Chl *c1*, as presented in Paper I. Chl *c1* is a porphyrin with an acrylic acid side chain, rather than a chlorin (see structure in Fig. 1), as most of the other chlorophylls are.[28] Close energetically and comparable in intensities, two electronic $Q_y$ and $Q_x$ transitions provided the means to observe signatures of weak vibronic coupling using polarisation-controlled 2DES.

# Bacteria under the scope of this work

The two main photosynthetic bacteria of this work are the purple bacterium *Rhodobacter sphaeroides* strain R-26 and the green bacterium *Chloroflexus aurantiacus* strain J-10-fl. Even though the two bacteria are only distantly related and contain somewhat different PSUs, they both possess type II reaction centres with potentially identical structures and achieve close to unity quantum yields for charge separation.[10,11]

## The purple bacterium *Rhodobacter sphaeroides*

The purple non-sulphur photosynthetic bacteria *Rhodobacter sphaeroides* (Fig. 2, left) are capable of growing in aerobic and anaerobic conditions, various temperatures, salinities up to 32 % and pH ranges between 3 to 11.[8] In addition, this bacteria also produce multiple bio-active substances, such as vitamin B12, coenzyme Q10 (ubiquinone), porphyrins and amino acids, which are helpful growth material for various plants, aquatic organisms and microorganisms.[29] These qualities and the relatively simple structure of its photosynthetic apparatus[17] have made the purple bacteria *Rhodobacter sphaeroides* one of the most thoroughly investigated species with remarkable versatility and metabolic significance.

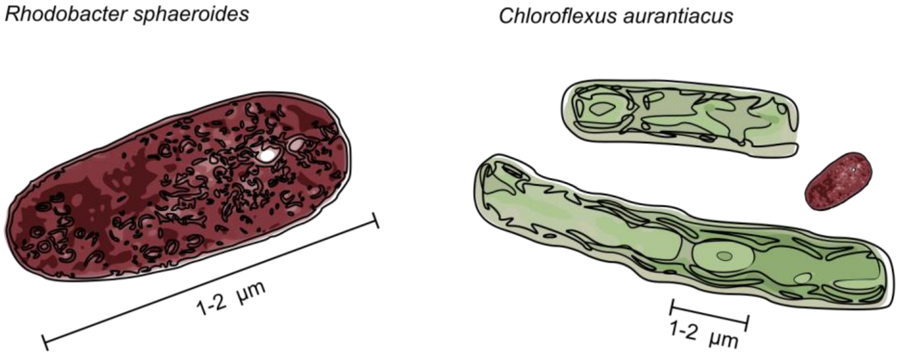

**Figure 2. Purple and green photosynthetic bacteria**
An illustrative figure of sizes and shapes of the purple bacterium *Rhodobacter sphaeroides* (left) and the green bacterium *Chloroflexus aurantiacus* (right). The size of monomeric units from both bacteria are several micrometres long,[16,30] yet the green bacteria tend to form long filaments with indefinite lengths.[31]

The PSU in purple bacteria *Rhodobacter sphaeroides* is likely the simplest photosynthetic apparatus found in nature.[17] It consists of only three types of pigment-protein complexes, all housed within the vesicles of the intracytoplasmic membrane, called chromatophores: two types of light-harvesting (LH) complexes, LH2 and LH1, and bacterial reaction centres (bRC).[32–34]The LH2 antenna is the dominant component in the PSU of purple bacteria that can form LH2-only domains for efficient energy capturing and transfer.[35] It consists of two overlapping rings, a weakly coupled B800 ring of 9 monomeric BChl *a* molecules and a strongly excitonically coupled B850 ring of 18 BChl *a* pigments.[35] The rings are embedded into a protein and carotenoid environment, where pigment-protein interactions control the properties and energy transfer between the B800-B850 rings.

The LH1-bRC is a joint system and exists in two shapes: S-shaped dimeric LH1 incorporating two bRCs inside each half-a-circle[30] and a monomeric C-shaped arrangement, identical to one-half of the dimeric one, with one bRC in the middle.[36] The S-shaped LH1 binds 56 BChls in dimeric subunits, while the C-shaped contains 28 BChls. With absorption around 875 nm, LH1 acts as an intermediate component in the LH2→LH1→bRC energy transfer scheme.[34,37]

In the membranes, the LH2 complexes surround the LH1-bRC systems. The overall LH2:LH1 (LH2:bRC) ratio within a single PSU varies depending on the light growing conditions, with an increasing ratio as illuminance decreases. Yet it was suggested that the ratio of 3:1 leads to the fastest and most efficient LH2→bRC EET.[34,38]

After photon absorption at LH2, energy is transferred between B800 molecules for a few hundred femtoseconds before being passed to the B850 ring.[13] The EET between the two rings (B800→B850) is temperature dependent, taking 0.7 ps at 300 K and 1.2 ps at 77 K.[39] It is followed by EET from B850 to LH1 at 4.6 ps.[40] The last EET from LH1 to bRC happens in around 35 ps, finalising the excitation transfer process through the entire PSU. The LH2→LH1 energy transfer can be direct (4.6 ps), or the energy might migrate in the pool of LH2 complexes for about 26 ps before the transfer to LH1.[40] This relatively slow diffusion process sets the overall energy transfer time in the PSU from the purple bacteria *Rhodobacter sphaeroides*.

The excitation energy trapping inside the *open* $\mathrm{bRC_{sph}}$ takes ~70 ps, while for the *closed* systems, the trapping time becomes longer and is around 200 ps.[37] The open/closed reaction centre terms define the state of the bRC system and whether it is ready to accept excitons from the antenna complexes. It is worth mentioning that trapping times here (and in other bRC) are not the direct EET from LH1 to the primary electron donor – a special pair. It is a time required for the reaction centre to secure the energy in a stable charge-separated state. The structures, EET and charge separation processes inside the $\mathrm{bRC_{sph}}$ (and $\mathrm{bRC_{cfx}}$) will be discussed in one of the upcoming sections.

## The green bacterium *Chloroflexus aurantiacus*

The *Chloroflexus aurantiacus* strain J-10-fl is a textbox example of filamentous, gliding, thermophilic, green photosynthetic bacteria, thriving in hots springs (optimal pH 8 and temperatures between 50-60°C) and capable of living either aerobically, anaerobically or semi-anaerobically.[31,41,42] In nature, the green bacteria tend to form long filaments of indefinite lengths,[31] creating a scattering nightmare to measure the optical properties of the species.

The PSU of *Chloroflexus aurantiacus* is slightly more complicated and consists of a chlorosome, a baseplate and a core antenna complex (B808-866-bRC). The chlorosome is a supramolecular organisation of thousands of primarily BChls *c* molecules, held together by long-distance pigment-pigment interactions[43,44] and forming rod-/lamellar-like aggregations inside an ellipsoidal lipid envelope.**24–26** The size of the chlorosome depends on the growth conditions and is on the order of 140-220 nm in length, 30-60 nm in width and 10-20 nm in thickness.[19] It operates as a light-harvesting organelle, absorbing photons and transferring excitation energy to the core complex via the baseplate.

The baseplate is a pigment-protein complex consisting of BChls *a*, carotenoids and multiple CsmA protein subunits. The complex is almost flat, with dimensions somewhat fixed in width (30-40 nm)[46] and thickness (3 nm)[19] but varying in length (60-200 nm) within the single cell.[46] It is positioned on one side of the chlorosome, linking it to the cytoplasmic membrane, where the core complex is located.[19]

The energy transfer ends in the membrane-bound core antenna complex: B808-866-bRC. The B808-866 complex is a ring-shaped antenna, biding three BChls *a* per molecular subunit and, similar to LH2, arranged in two spectrally distinct groups, monomeric B808 and excitonically coupled B866.[47,48] The circle's diameter is around 10 nm, and, similar to the LH1-bRC system in purple bacteria, the bRC is located in the centre of it.[47,48]

The downhill EET from the chlorosome to the core complex via the baseplate proceeds in tens of picoseconds (~50 ps).[22] It is followed by a relatively fast energy transfer step of 2 ps between two bands of the B808-866 complex.[49] The excitation energy trapping in the photochemically active bRC takes tens of picoseconds (43 ps[50] or 70-90 ps[22]) but can take up to 200 ps for *closed* systems.[22] In addition, the energy transfer efficiency between the chlorosome and core complex in *Chloroflexus aurantiacus* was reported to be temperature dependent. It was estimated to be near 100% close to its growth temperatures (> 40°C), but as low as 15% at 4 K.[51] To determine the precise times of EET and energy capture in intact PSU, we performed 2DES on the intact cells of the green bacterium *Chloroflexus aurantiacus* at room temperature (Paper V). Excitations to various parts of the PSU allowed us to draw the step-by-step EET scheme and determine the exact trapping time inside the open bRCs.

## Bacterial reaction centres

Bacterial reaction centres are essential pigment-protein complexes performing charge separation and assisting in excitation energy trapping. With the comprehensive spectroscopic research data and the structure known from X-ray crystallography,[52] the bRC$_{\mathrm{sph}}$ from the purple bacteria is a foothold to examine other reaction centres. For example, when studying bRC$_{\mathrm{cfx}}$, which structure is unknown, the two reaction centres are often compared.[53–57] Most of the conclusions drawn about bRC$_{\mathrm{cfx}}$ in this thesis also come from the consideration that the systems and optical properties of the two bRCs are very similar. In this subchapter, the two reaction centres are also presented in parallel.

### *Structure*

The structure of bRC$_{\mathrm{sph}}$ is presented on the left side of Fig. 3. Embedded between three separate polypeptide chains, designated according to their molecular weights as $L$ (light), $M$ (medium) and $H$ (heavy), the complex itself consists of eight active constituents: four BChls $a$, two bacteriopheophytins $a$ (BPheo) and two quinones.[52] The eight co-factors are arranged into two nearly symmetric branches, marked with indexes ‘A’ and ‘B’. Two BChl pigments form a strongly excitonically coupled dimer – a ‘special pair’ ($P$). The special pair – the primary electron donor – is flanked by two accessory BChls ($B_A$ and $B_B$), two BPheos ($H_A$ and $H_B$) and two electron acceptors – quinones ($Q_A$ and $Q_B$).

The exact structure of bRC$_{\mathrm{cfx}}$ has yet to be established, but it is the simplest type II reaction centre known so far.[58] The structure, as presented on the right side of Fig. 3, was adapted from the structure of bRC$_{\mathrm{sph}}$ according to the following changes. The bRC$_{\mathrm{cfx}}$ is known to contain only two protein subunits, very similar to the $L$ and $M$ subunits of bRC$_{\mathrm{sph}}$.[59,60] From the comparison of bRC$_{\mathrm{sph}}$ and bRC$_{\mathrm{cfx}}$ absorption spectra[54] and the early pigment extraction and composition studies,[53] the ratio between BChls and BPheos in bRC$_{\mathrm{cfx}}$ was predicted to be 1:1, leading to the system of three BChls and three BPheos. It was suggested, that the third BPheo replaces the accessory BChl in the ‘B’ branch ($\phi_B \rightarrow B_B$).[61] The claim was confirmed from low temperature 2DES data of quinone-reduced bRC$_{\mathrm{cfx}}$ in Paper IV. Lastly, the electron acceptors in bRC$_{\mathrm{cfx}}$ are two menaquinones instead of quinones.[62]

After introducing the bRC structure, it is worth exploring the definitions of the open/closed reaction centres in more detail. The open reaction centre is in its neutral state, while in the closed system, either the special pair of the bRC is oxidised ($P^+$) and/or a quinone in an active branch is reduced ($Q_A^-$).[22,37]

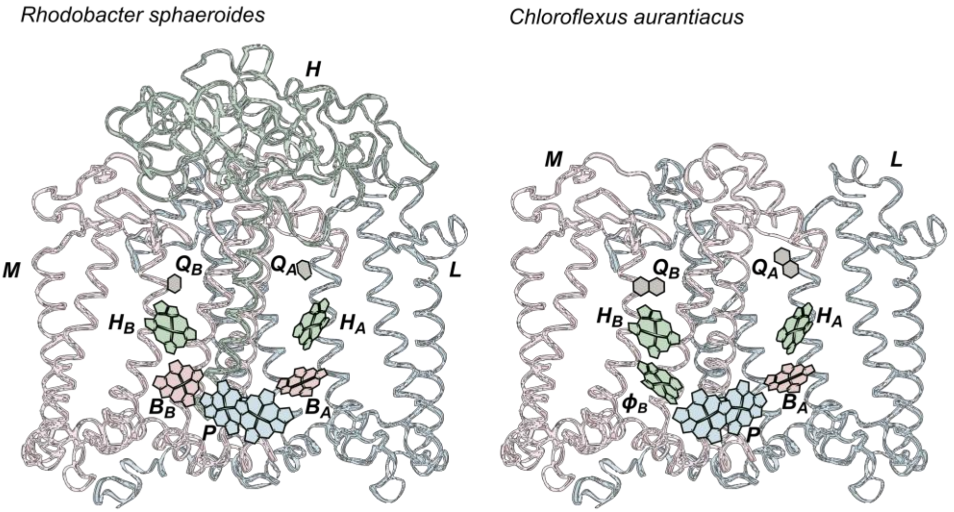

**Figure 3. Structures of bacterial reaction centres**
The bacterial reaction centre from purple bacteria bRC$_{\mathrm{sph}}$ (left) is a pigment-protein complex embedded between three protein chains: $L$, $M$ and $H$, and consisting of eight photo-active co-factors: four BChls ($B_A$, $B_B$ and a strongly excitonically coupled BChl dimer – $P$), two BPheos ($H_A$ and $H_B$) and two quinones ($Q_A$ and $Q_B$). The co-factors are grouped into two branches, 'A' and 'B'. The structure of bRC$_{\mathrm{cfx}}$ from green bacteria (right) lacks one protein chain ($H$), and BChl in the B branch is substituted by BPheo ($\phi_B \rightarrow B_B$). In addition, the main electron acceptors in bRC$_{\mathrm{cfx}}$ are two menaquinones.[62] The structure of bRC$_{\mathrm{sph}}$ was drawn from X-ray crystallography data,[52] and the structure of bRC$_{\mathrm{cfx}}$ was adjusted from the same data according to the mentioned changes. These and other structures in this thesis were drawn with VMD software. VMD is developed with NIH support by the Theoretical and Computational Biophysics group at the Beckman Institute, the University of Illinois at Urbana-Champaign.[63]

### *Excitation energy and electron transfer processes*

The bacterial reaction centre is a unique system undergoing excitation energy transfer (EET) and electron transfer (ET) processes. After a photon absorption and a 'downhill' EET along both branches to the primary electron donor (the special pair, $P$), an electron is transferred from the donor to the primary electron acceptor ($Q_A$) through just one, an 'active' branch, as indicated with index 'A' in Fig. 3.[64]

The internal charge separation inside bRCs leads to the creation of cation ($P^+$) and anion ($H_A^-$ or $Q_A^-$) molecules which generate an internal electric field. The energy of molecules that fall into the field – the accessory BChls ($B_A$ and $B_B$) for bRC$_{\mathrm{sph}}$ or accessory BChl and BPheo ($B_A$ and $\phi_B$) for bRC$_{\mathrm{cfx}}$ – shifts. The effect is known as an electrochromic shift or Stark effect.[64–67]

In time-resolved spectroscopy, the electrochromic shift appears as a time-dependent derivative-shaped signal, consisting of a positive peak transforming rapidly to a negative one.[64–67] It is common to refer to this signal as a *dynamic band-shift signal*. The appearance of the dynamic band-shift signal in bRCs allows direct observations of the internal charge separation process in the intact systems through the spectroscopic changes of the individual co-factors.[68,69]

In the purple bRC$_{sph}$, EET through the co-factors to the special pair happens in ~100 fs.[70,71] The electron transfer to $H_A$ takes a time of 2.8 ps at 300 K[72] and 1.5 ps at 77 K.[73,74] To reach the primary electron acceptor, $P^+H_A^- \rightarrow P^+Q_A^-$, then takes around 200 ps.[75,76]

The involvement of accessory BChl ($B_A$) in the ET process was a matter of debate for quite some time, as the transient spectroscopy measurements failed to observe the formation of the $P^+B_A^-$ state. It was suggested that the creation of the $P^+B_A^-$ state was ~3 times slower than depopulation (~3 ps versus ~1 ps),[76] which made the state's spectroscopic signatures undetectable with the time-resolved experiments.

The EET and ET steps in bRC$_{cfx}$ are overall slower than those of bRC$_{sph}$. The EET happens with a similar characteristic time of hundreds of femtoseconds (Paper IV). The initial charge separation step $P^* \rightarrow P^+H_A^-$ proceeds with 7.1 ps at physiological temperatures, while at 80 K, the kinetics become non-exponential, with two characteristic times of 3.1 ps and ~32 ps.[77] From the $P^+H_A^-$ state, reaching primary electron acceptor, $P^+Q_A^-$, takes around 365 ps.[78]

Despite more than 50 years of research and books summarising and reviewing the scientific research on photosynthetic bacteria and their complexes, several open questions remain. One technical question, discussed extensively in Paper II, was observing and describing dynamic band-shift signal in 2DES. The dispersive shape of the signal in transient absorption experiments can be understood rather intuitively as a subtraction of the initial absorption pattern from the absorption spectrum with the Stark-shifted transitions. However, in 2DES, all this intuition is lost, as the excited system emits the recorded signal, and no subtraction of the signals is done. To describe the electrochromic band shifts in 2DES, we introduced a new class of double-sided Feynman diagrams, called *re-excitation* (Paper II).

Another unresolved discussion concerns low-lying charge-transfer states in bacterial reaction centres. The double structure of the main absorption band of the special pair at cryogenic temperatures was observed and discussed on a few occasions for various bRCs.[79–83] It was postulated that it could be a charge transfer (CT) state below the lowest-energy excitonic state of the special pair dimer.[79] However, a different opinion settled that the double feature originated from the structural inhomogeneities within the samples.[84] Nevertheless, variations in the sample composition cannot explain the duality of the absorption band observed in several reaction centres (e.g. *Rhodobacter sphaeroides, Rhodobacter viridis, Allochromatium vinosum*). [79,81,82] We revisited this claim in Papers III and IV by performing 2DES experiments at cryogenic temperatures on bRC$_{sph}$ and bRC$_{cfx}$ and provided spectroscopic evidence for the charge transfer states in the special pair band.

In addition, there is still an ongoing debate about the positions of higher excitonic transitions of the special pair in $bRC_{sph}$ and $bRC_{cfx}$, confounded by many different studies and findings.[54,61,85] The weak dipole moment of the higher excitonic transition and the extremely fast relaxation between the two excitonic states made it challenging to determine the exact position of the higher state. We reassessed this topic in Paper II for $bRC_{sph}$ and Paper IV for $bRC_{cfx}$ and defined the positions of the higher energy excitonic states of the special pairs in both bRCs.

Lastly, the two time components for charge separation in $bRC_{cfx}$ and their ratio reported in the literature differ significantly; see references [57,77,86]. There is also no common conclusion as to why the dynamics at low temperatures become non-exponential in the first place.[77] To clarify this, we performed a 2DES study on the quinone-reduced $bRC_{cfx}$ at 78 K, presented in Paper IV. The femtosecond time resolution allowed us to separate the two time components and propose an explanation for the dual origin of charge separation.

# Two-dimensional electronic spectroscopy

This chapter aims to provide basic knowledge about two-dimensional electronic spectroscopy (2DES) – the main experimental technique used in this thesis. It begins with an overview of 2DES, followed by the three main subchapters that briefly introduce theoretical formalism, provide ways to track signal evolution and cover a few experimental nuances. The goal of this chapter is not to write down a complete theory behind the 2DES nor to give step-by-step instructions on how to perform an experiment. It should contain a summary of important aspects necessary to understand the experimental data and photo-induced processes presented in this thesis. For more information, we refer to field-famous books [87–89] or detailed review papers [90–92].

## 2DES – a long story short

Two-dimensional electronic spectroscopy belongs to a family of so-called transient four-wave mixing (TFWM) experiments. During the experiment, three laser pulses interact with the sample, exciting it to various energy states and producing an emitted signal. Controlling time delays between these pulses allows to follow and record the system's evolution after excitation. The main goal of 2DES experiments is to collect emitted signals with respect to these delay times. To do so, it is necessary to handle the timing of laser pulses with extremely high accuracy.

There are many methods to achieve the experimental requirements mentioned above; see references [91,93–95]. But in this thesis, only a 2DES in a non-collinear heterodyne detection geometry will be presented. The temporal and spatial arrangements of the four non-collinear laser pulses, as manipulated during 2DES experiments, are pictured in Fig. 4.

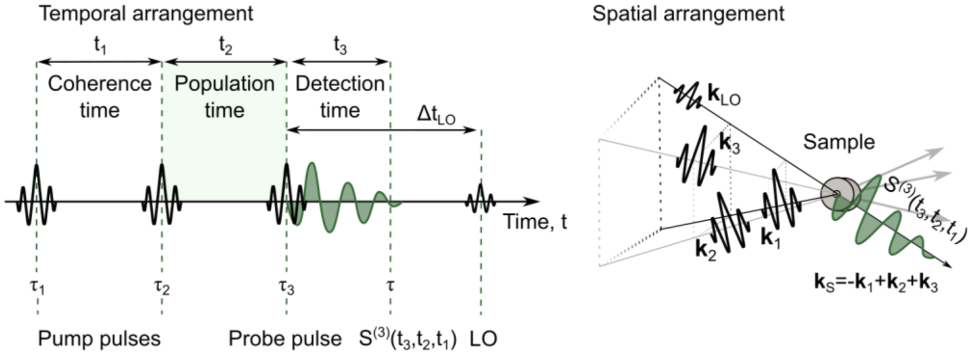

**Figure 4. Temporal and spatial arrangements of four laser pulses in 2DES experiments**
During 2DES experiments in a box-CARS geometry, three laser pulses arrive at the sample from the three corners of an imaginary box and interact with the sample at $\tau_1, \tau_2$ and $\tau_3$ time moments. The signal radiated to the specific phase-matching direction $\mathbf{k}_S = -\mathbf{k}_1 + \mathbf{k}_2 + \mathbf{k}_3$ is called a photon echo (PE). It propagates together with the local oscillator (LO) pulse along the pathway of a fourth corner of a box. The LO is usually delayed from the third laser pulse (and the signal) by some delay time, $\Delta t_{LO}$, which in our case is 2.57 ps. The third-order signal can be characterised as a function of delays between the laser pulses, $t_1$ and $t_2$, and a detection time $t_3$, as $S^{(3)}(t_3, t_2, t_1)$.

In time, three pulses interact with the sample at $\tau_1, \tau_2, \tau_3$ time moments. The first two pulses are noted as pump pulses, and the third as a probe pulse. The delay between the pump pulses, $t_1 = \tau_2 - \tau_1$, is called coherence time, and the delay between the second pump and the probe pulse, $t_2 = \tau_3 - \tau_2$, is called population time. The fourth, weaker pulse is a so-called local oscillator (LO). The LO is there for the heterodyne detection of the signal.[88]

In space, four laser pulses arrive at the sample non-collinearly, arranged in a square shape. This particular experimental geometry, where three laser pulses make up three corners of a square with the signal emitted on the fourth corner, is usually referred to as a box-CARS. Interactions with three pulses with wavevectors $\mathbf{k}_1$, $\mathbf{k}_2$, and $\mathbf{k}_3$ induce a third-order polarisation in the sample. The sample later radiates electric fields in multiple phase matching directions $\pm\mathbf{k}_1 \pm \mathbf{k}_2 \pm \mathbf{k}_3$. The so-called photon echo (PE) signal is exclusively generated in the $\mathbf{k}_S = -\mathbf{k}_1 + \mathbf{k}_2 + \mathbf{k}_3$ direction and propagates in the fourth corner of 'the box' together with the fourth pulse, the LO.[88]

In practice, it is common to collect two different signals from the PE, or the rephasing ($\mathbf{k}_R = -\mathbf{k}_1 + \mathbf{k}_2 + \mathbf{k}_3$) pulse sequence and the non-rephasing pulse sequence ($\mathbf{k}_{NR} = +\mathbf{k}_1 - \mathbf{k}_2 + \mathbf{k}_3$). The so-called purely absorptive spectrum can then be plotted as the real part of the rephasing and non-rephasing signals (see, for example, ref. [88] for a detailed explanation). Since the two pump pulses are identical (apart from their directions of propagation), when measuring in the box-CARS geometry, both signals can be generated by simply changing the time order between

$\mathbf{k}_1$ and $\mathbf{k}_2$ pulses and collecting the signal in the same $\mathbf{k}_\mathrm{S}$ direction. When $\mathbf{k}_1$ pulse arrives first, the rephasing signal is generated, and when $\mathbf{k}_2$ comes first, the non-rephasing signal is emitted in the $\mathbf{k}_\mathrm{S}$ direction.

The boc-CARS heterodyne detection scheme has a few major advantages. Two time-separated pump pulses decouple excitation frequency from the time resolution using Fourier transform (FT) approach. This means that laser pulses can be as short as possible without the expense of spectral resolution. In addition, the box-CARS geometry is formally background-free since the signal's direction differs from the direction of excitation pulses. Finally, as discussed in the upcoming sections, non-collinear propagation enables individual manipulation of four laser pulses and the application of a heterodyne detection scheme to facilitate the detection of very weak signals.

## The brief theory behind the response function formalism

This subchapter presents a small part of the theory and the main equations behind TFWM experiments. The introduction starts with a well-known Hamiltonian for a system interacting with an incident electric field and finishes with eight members of the third-order response function. A detailed theoretical approach can be found in references [87,89,90].

### Hamiltonian of a system

The Hamiltonian of a system – an operator defining its' total energy – which is surrounded by a harmonic environment (a bath) and also interacts with an external electric field, can be written as a sum of two separate Hamiltonians:

$$\hat{H} = \hat{H}_\mathrm{syst} + \hat{H}_\mathrm{int}(t). \tag{1}$$

In this formulation, the first part of the Hamiltonian contains everything about the system (S), its harmonic bath (B), which causes dephasing and relaxation, and their system-bath interaction (SB): $\hat{H}_\mathrm{syst} = \hat{H}_\mathrm{S} + \hat{H}_\mathrm{B} + \hat{H}_\mathrm{SB}$. The second, time dependent term, $\hat{H}_\mathrm{int}(t)$, describes a dipolar system-field interaction – a system's perturbation by an external electric field.

After the dipole approximation, assuming that the size of the molecular system is smaller than the optical wavelength of the incident electric field, the interaction term can be written as a scalar product of two vectors:

$$\hat{H}_\mathrm{int}(\mathrm{t}) = -(\hat{\boldsymbol{\mu}} \cdot \boldsymbol{E}(\boldsymbol{r}, t)). \tag{2}$$

Here, $\boldsymbol{E}(\boldsymbol{r}, t)$ is the incoming electric field, and $\hat{\boldsymbol{\mu}}$ is the electric dipole moment operator.

The incoming optical electric field induces a nonlinear polarisation in the system. Mathematically, the property is defined as a convolution of the external electric field with a time-dependent electrical (optical) susceptibility term ($\chi(t)$), multiplied by a vacuum permittivity, $\varepsilon_0$:

$$P(t) = \varepsilon_0 \int_{-\infty}^{+\infty} \chi(t - t')E(t')\, dt'. \tag{3}$$

In Eq. (3), the susceptibility, which in reality is a tensor, was replaced by a constant, assuming the interacting medium is isotropic and non-dispersive, and vector notations of polarisation and electric fields were dropped with an assumption polarisation of the electric dipole moment operator and that of the incident electric field are parallel.

The induced nonlinear polarisation can be expanded using the Taylor series in terms of the different orders of nonlinearity:

$$P(t) = P^{(1)}(t) + P^{(2)}(t) + P^{(3)}(t) + \cdots. \tag{4}$$

The various terms from the above expression define responses from the system after certain interactions. For example, the linear polarisation term $P^{(1)}(t)$ is essential for defining linear absorption. The expression can be written through the linear response function $S^{(1)}(t_1)$ as follows:

$$P^{(1)}(t) = \int_0^{\infty} \mathrm{d}t_1\, S^{(1)}(t_1)E(t - t_1). \tag{5}$$

For the TFWM experiments, the third-order polarisation term $P^3(t)$ needs to be considered since it is defined by three interactions with the incoming electric fields. The third-order polarisation can be written as:

$$\begin{aligned} P^{(3)}(t) = \int_0^{\infty} \mathrm{d}t_3 \int_0^{\infty} \mathrm{d}t_2 \int_0^{\infty} \mathrm{d}t_1\, S^{(3)}(t_3, t_2, t_1) \\ E(t - t_3)E(t - t_3 - t_2)E(t - t_3 - t_2 - t_1). \end{aligned} \tag{6}$$

The time notations, $t_1, t_2, t_3$, mark time variables for the response function – periods between the system-field interactions – as indicated in Fig. 4. Equations (5) and (6) are again the convolutions of the response function and external electric field functions, $E(t)$. From the analogy of Eq. (3) and Eqs. (5) and (6), it becomes clear that the response functions carry all the information about the system's optical properties.

When it comes to experiments in the *homodyne* detection scheme, the measurement directly probes the signal intensity ($I_{sig}$). The intensity has a quadratic dependence on the emitted electric field, $E_{sig}(t)$, and, in turn, is directly proportional to the induced polarisation, $P(t)$:

$$I_{sig} \propto \left|E_{sig}(t)\right|^2 \propto |P(t)|^2. \tag{7}$$

For the *heterodyne* detection scheme, as in our case, the detector measures an interference between the emitted electric field and the fourth laser pulse, the LO. The detected intensity is then:

$$\begin{aligned} I_{sig} &\propto \left|E_{LO}(t) + E_{sig}(t)\right|^2 \\ &= |E_{LO}(t)|^2 + \left|E_{sig}(t)\right|^2 + 2Re[E_{LO}^*(t)E_{sig}(t)]. \end{aligned} \tag{8}$$

The first two terms of this expression can be neglected, as the signal's term ($\left|E_{sig}(t)\right|^2$) alone is relatively weak, and the LO pulse can be subtracted if desired. What remains is the cross-term, which allows measuring the phase and time dependence of the signal $E_{sig}(t)$ relative to $E_{LO}(t)$. Equation (8) suggests that measuring the emitted signal (knowing the time dependence of the induced nonlinear polarisation) is sufficient to extract essential information about the optical properties of the system.

## Third-order response function

Response functions are calculated using perturbation theory, a rather involving and sophisticated theoretical approach. The details behind the method can be found in ref. [89], and here only the final result, essential for understanding 2D spectra, is given.

The total response function can be written as a sum of individual response functions ($R_\alpha$), describing various system-field interactions. For the TFWM experiments, the total third-order response of the system interacting with three laser pulses can be re-written as a sum of eight members:

$$S^{(3)}(t_3, t_2, t_1) = \Theta(t_3)\Theta(t_2)\Theta(t_1)\sum_\alpha^8 R_\alpha(\tau, \tau_1, \tau_2, \tau_3). \tag{9}$$

The Heaviside functions, $\Theta(t)$, which are equal to one if $t > 0$ and to zero if $t < 0$, ensure the system-field interactions take place in a correct time order. The relationships between the interaction and evolution times are $\tau = t$, $\tau_3 = t - t_3$, $\tau_2 = t - t_3 - t_2$, $\tau_1 = t - t_3 - t_2 - t_1$, as it was indicated in Fig. 4.

Eight members of Eq. (9) are:

$$
\begin{aligned}
R_1(\tau;\tau_1,\tau_2,\tau_3) &= +\mathrm{Tr}[\hat{\mu}(\tau)\hat{\mu}(\tau_3)\hat{\boldsymbol{\rho}}_{\boldsymbol{eq}}\hat{\mu}(\tau_1)\hat{\mu}(\tau_2)],\\
R_2(\tau;\tau_1,\tau_2,\tau_3) &= +\mathrm{Tr}[\hat{\mu}(\tau)\hat{\mu}(\tau_2)\hat{\boldsymbol{\rho}}_{\boldsymbol{eq}}\hat{\mu}(\tau_1)\hat{\mu}(\tau_3)],\\
R_3(\tau;\tau_1,\tau_2,\tau_3) &= -\mathrm{Tr}[\hat{\mu}(\tau)\hat{\mu}(\tau_3)\hat{\mu}(\tau_2)\hat{\boldsymbol{\rho}}_{\boldsymbol{eq}}\hat{\mu}(\tau_1)],\\
\\
R_4(\tau;\tau_1,\tau_2,\tau_3) &= +\mathrm{Tr}[\hat{\mu}(\tau)\hat{\mu}(\tau_3)\hat{\mu}(\tau_2)\hat{\mu}(\tau_1)\hat{\boldsymbol{\rho}}_{\boldsymbol{eq}}],\\
R_5(\tau;\tau_1,\tau_2,\tau_3) &= +\mathrm{Tr}[\hat{\mu}(\tau)\hat{\mu}(\tau_1)\hat{\boldsymbol{\rho}}_{\boldsymbol{eq}}\hat{\mu}(\tau_2)\hat{\mu}(\tau_3)],\\
R_6(\tau;\tau_1,\tau_2,\tau_3) &= -\mathrm{Tr}[\hat{\mu}(\tau)\hat{\mu}(\tau_3)\hat{\mu}(\tau_1)\hat{\boldsymbol{\rho}}_{\boldsymbol{eq}}\hat{\mu}(\tau_2)],\\
\\
R_7(\tau;\tau_1,\tau_2,\tau_3) &= -\mathrm{Tr}[\hat{\mu}(\tau)\hat{\boldsymbol{\rho}}_{\boldsymbol{eq}}\hat{\mu}(\tau_1)\hat{\mu}(\tau_2)\hat{\mu}(\tau_3)],\\
R_8(\tau;\tau_1,\tau_2,\tau_3) &= -\mathrm{Tr}[\hat{\mu}(\tau)\hat{\mu}(\tau_2)\hat{\mu}(\tau_1)\hat{\boldsymbol{\rho}}_{\boldsymbol{eq}}\hat{\mu}(\tau_3)].
\end{aligned}
\tag{10}
$$

The density matrix, $\hat{\boldsymbol{\rho}}_{\boldsymbol{eq}}$, which describes the state of the system, is written in bold here to highlight its relative position in the expansions. The upcoming subchapter is dedicated to understanding these expressions and showing how mathematical equations can be connected to visible signals.

## Tracking 2DES signals

The following subchapter overviews various ways to track, represent and understand third-order signals. It picks six essential members from the third-order response function ($R_1$ to $R_6$, Eq. (10)) and presents them in the useful visual representation of double-sided Feynman diagrams. The later sections summarise the construction and interpretation of a 2D spectrum, followed by a discussion about various 2DES signals and their constructive/destructive interference.

### Conventional double-sided Feynman diagrams

As it will become clear at the end of this section, expressions $R_1$ to $R_6$ contain all the essential system–field interactions during the time period of interest. However, they are densely packed and challenging to read. At this point, it is natural to introduce the so-called double-sided Feynman diagrams. They provide a visual picture of interactions described by Eq. (10) and serve as a convenient tool to track the system's evolution. Details for drawing these diagrams can be found elsewhere [88] and will be only briefly discussed here.

The six conventional double-sided Feynman diagrams (Fig. 5) show the single molecule's evolution in the density matrix representation, $\hat{\rho}_{eq} = |g_1\rangle\langle g_1|$. Vertical lines correspond to the time evolution, which runs upwards, and the black arrows indicate system-field interactions. The levels of the system are noted as follows: $g_1$ – a ground state, $e_1$ – an excited state, $f_1$ – a two-exciton state.

The interactions with the *ket* ($|g_1\rangle$, left side) or *bra* ($\langle g_1|$, right side) vectors of the density matrix and the interaction time order are all 'encoded' in the expressions $R_1$ to $R_6$. They can be determined from the positions of transition dipole moments relative to the density matrix and their time notations. E.g. the $\hat{\boldsymbol{\rho}}_{\boldsymbol{eq}}\hat{\mu}(\tau_1)$ part in $R_1$ expression describes the first interaction with the *bra* vector of the density matrix ($|g_1\rangle\langle \boldsymbol{g_1}| \leftarrow$) at the time $\tau_1$, as indicated by a first black arrow ($\mathbf{k}_1$) positioned on the right side of the $R_1$ diagram in Fig. 5.

In addition, the black arrow pointing to the left (←) corresponds to an interaction with the electric field with $e^{i\omega t - i\boldsymbol{kr}}$ phase factor, and an arrow pointing to the right (→), with $e^{-i\omega t + i\boldsymbol{kr}}$. These wavevectors are described by two phase matching directions: rephasing ($\mathbf{k}_\mathrm{R} = -\mathbf{k}_1 + \mathbf{k}_2 + \mathbf{k}_3$) and non-rephasing ($\mathbf{k}_\mathrm{NR} = +\mathbf{k}_1 - \mathbf{k}_2 + \mathbf{k}_3$).

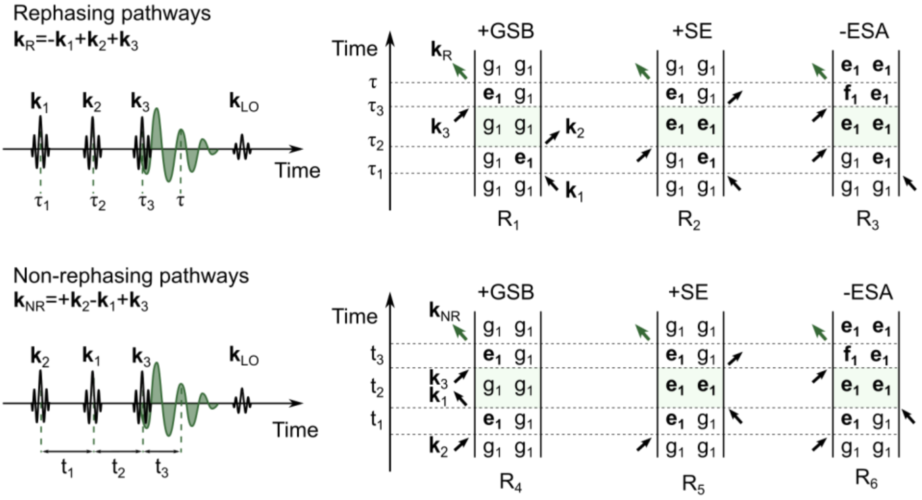

**Figure 5. Feynman diagrams for rephasing and non-rephasing pulse order**
Rephasing ($\mathbf{k}_\mathrm{R} = -\mathbf{k}_1 + \mathbf{k}_2 + \mathbf{k}_3$, top) and non-rephasing ($\mathbf{k}_\mathrm{NR} = +\mathbf{k}_1 - \mathbf{k}_2 + \mathbf{k}_3$, bottom) double-sided Feynman diagrams represent six possible laser-matter interaction pathways: ground state bleaching (GSB), stimulated emission (SE) and excited state absorption (ESA). The levels of the system are noted as follows: $g_1$ – a ground state, $e_1$ – an excited state, and $f_1$ – a two-exciton state of the same molecule. For clarity, the bra/ket notations are omitted in the density matrix representation. Note that when pulses $\mathbf{k}_1$ and $\mathbf{k}_2$ are interchanged in time, the non-rephasing signal is generated in the same phase-matching direction as the rephasing signal.

Furthermore, the arrow pointing towards the vertical line indicates absorption and pointing away shows emission from the system. The last interaction is, by convention, emission from the system and always points away from the left side of the diagram (green arrow). After all four interactions, the system must end up either in the ground ($|g_1\rangle\langle g_1|$) or in the excited ($|e_1\rangle\langle e_1|$) population state.

The $R_1$ to $R_6$ members in Eq. (10) are numbered as conventional time-resolved spectroscopy signals for rephasing and non-rephasing phase matching directions. These are ground state bleaching (GSB – $R_1$ and $R_4$), stimulated emission (SE – $R_2$ and $R_5$) and excited state absorption (ESA – $R_3$ and $R_6$) contributions. The last two members ($R_7$ and $R_8$) do not produce any signals in the detected phase-matching direction.

Lastly, the overall sign of the signal, described by each diagram, is determined by the number of right-side interactions. It is positive if the number of interactions is even (GSB and SE) and negative if it is odd (ESA).

Looking into the evolution of the density matrix, the first interaction creates optical coherence between the ground and excited states ($|g_1\rangle\langle e_1|$) or ($|e_1\rangle\langle g_1|$). In terms of population dynamics, the second interaction produces a population in the ground ($|g_1\rangle\langle g_1|$) or excited ($|e_1\rangle\langle e_1|$) states. The third interaction with the laser pulse then again generates coherence between the ground and excited ($|e_1\rangle\langle g_1|$) or between two excited states ($|f_1\rangle\langle e_1|$). This final state produces (emits) the third-order signal, as indicated by the fourth arrow in the double-sided Feynman diagrams in Fig.5.

In addition to the Feynman diagrams covering population dynamics, the quantum beatings signals (QB, omitted from Fig. 5) describe oscillating signals and are used to monitor coherences in the system. For the QB signals, the second interaction creates coherence either in the ground ($|g_1\rangle\langle g_1{}'|,\ g_1 \neq g_1{}'$) or in the excited ($|e_1\rangle\langle e_1{}'|,\ e_1 \neq e_1{}'$) states. Coherences in the ground state are solely vibrational, while coherences in the excited state can be of electronic or vibronic (excited state vibrational) origins.[96,97] These coherences are visible as oscillatory signals during population time, with frequencies corresponding to the energy difference between the two states involved.

## Constructing a two-dimensional spectrum

The third-order signal can be rather naturally represented as a time-resolved 2D spectrum with one axis representing the excitation and the other one – detection energies. For this, the recorded signal, $S(\tilde{\nu}_3', t_2, t_1)$, which is a set of interferograms between the emitted electric field and the LO pulse, is converted to a 2D spectrum by an FT over coherence time ($t_1 \to \tilde{\nu}_1$) and a back and forward FT and windowing over $\tilde{\nu}_3'$ dependency: $\tilde{\nu}_3' \ \to t_3 \cdot w(t) \to \tilde{\nu}_3$. Here $w(t)$ is a window function in the time domain. The result is a correlation spectrum between excitation ($\tilde{\nu}_1$) and detection ($\tilde{\nu}_3$) wavenumbers for a fixed population (evolution) time, $t_2$.

One of the many ways to present a 2D spectrum is shown in Fig. 6. The excitation axis is horizontal and increases from left to right, while the detection axis is vertical and grows from the bottom to the top. There is still no general agreement on the best way to plot 2D spectra. Sometimes the spectra are plotted with transposed excitation and detection axes or using wavelength or eV instead of frequency. Yet this defines only the graphical interpretation of the signal, while the information obtained from 2DES experiments is the same.

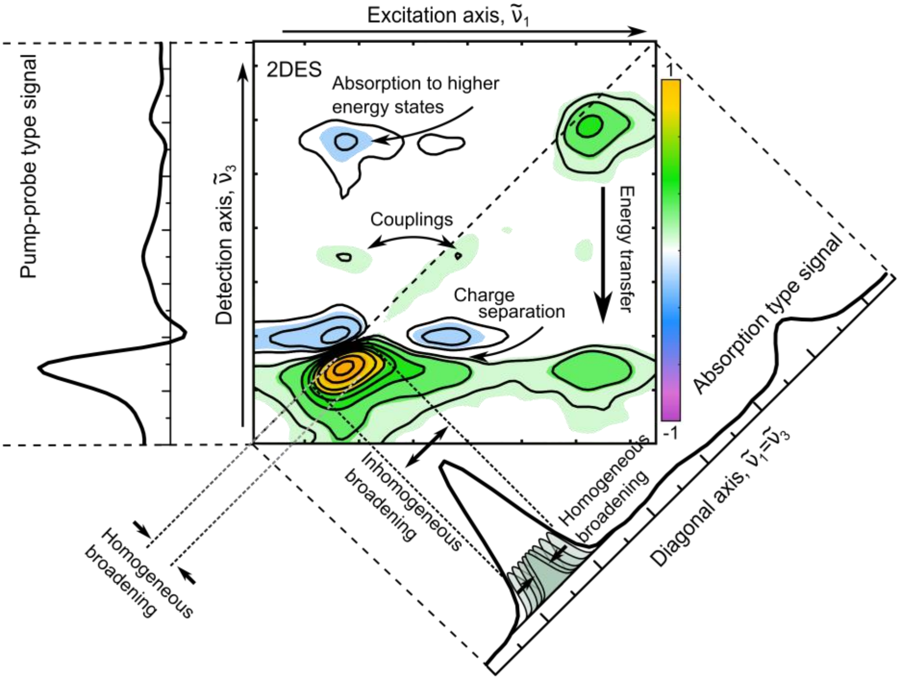

**Figure 6. 2D spectrum and the information it carries**

Example of an absorptive part of the total (rephasing+non-rephasing) 2D spectrum and the information it carries. At early population times, diagonal cut corresponds to absorption type signals, and homogeneous and inhomogeneous broadenings correlate with diagonal and anti-diagonal widths of the diagonal 2D peaks. The position of diagonal peaks indicates molecular transitions, while cross-peaks correspond to couplings or excitation energy transfer. Negative signals usually stand for absorption to higher energy states, yet in specific systems, such as bRCs, it can also indicate charge separation. The integrated signal over the excitation axis can be scaled to match pump-probe-type signals at various population times.

Positions of the particular signals in the 2D spectrum, as described by double-sided Feynman diagrams in Fig. 5, are defined by the first interaction (absorption ≡ excitation energy) and the last interaction (emission ≡ detection energy). As already mentioned, peaks with positive amplitude rise from the ground state bleaching and stimulated emission signals. Negative features indicate the excited state absorption or re-excitation processes (see further section).

Many things can be learned and determined from 2D spectra. The positions of the peaks and cross-peaks indicate various transitions: electronic, vibrational or vibronic.[96,97] Homogeneous and inhomogeneous broadenings of lineshapes can also be extracted from the shape of diagonal peaks. Homogeneous broadening – defined by molecular properties, such as population relaxation, pure dephasing or orientation relaxation – corresponds to an anti-diagonal width of the 2D peak. While inhomogeneous broadening – relatively wide energy distribution of electronic transitions, resulting from the distribution of molecular interactions with the environment (solvent, proteins, etc.) – corresponds to the diagonal width of the diagonal 2D peak.

From the changes in 2D signal during population time, dynamics of various photo-induced processes can be obtained. For example, the evolution of lineshapes of diagonal peaks provides information about intraband processes[98,99] or environmental effects.[100] The cross-peaks, on the other hand, carry information about couplings and excitation energy transfer between the states.[101,102] The charge separation and electron transfer can be monitored through the emerging signals from charged molecules or the formation of dynamic band-shift signals (Paper II). Lastly, patterns and lifetimes of coherent signals, combined with polarisation control of the laser pulses, can help to determine the origin of the transitions [96,97,103,104] and couplings between the states (Paper I).

## 2D spectra for various systems: introducing re-excitation pathways

In a way they were formulated in the previous section, the Feynman diagrams describe light-matter interactions within a single molecule. Naturally, light-harvesting systems are much more complicated. To develop a full and clear picture of how molecular interactions are reflected in 2DES, we distinguished specific signals from $R_3$ and $R_6$ pathways (ESA diagrams) as a new group of Feynman diagrams. We called them *re-excitation* (RE) pathways. The RE pathways cover signals originating from two or more molecules or the same molecule after EET/ET and molecular relaxation. The RE signals were introduced in Paper II to disentangle the formation of dynamic band-shift signals in $\text{bRC}_{\text{sph}}$. Yet, it is essential to note that several groups had used similar diagrams before (called negative GSB or simply ESA) to explain excitonic delocalisation or EET dynamics.[101,102,105]

To illustrate the need and practicality of RE diagrams, a simple case of a weakly coupled molecular dimer is presented in Fig. 7. The ‘weak’ coupling means that molecular interaction does not change energy states ($e_1, e_2$, where $e_2 > e_1$) nor transitions ($\mu_1, \mu_2$) of two molecules, however, Förster resonance energy transfer (excitation energy transfer, EET, $e_2 \rightarrow e_1$) is present.

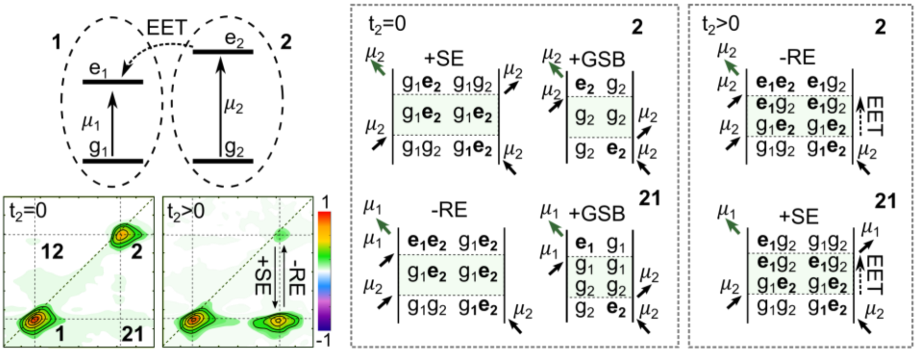

**Figure 7. 2DES of a weakly coupled dimer**
Scheme of energy states for a weakly coupled heterodimer together with two 2D spectra before ($t_2 = 0$) and after ($t_2 > 0$) excitation energy transfer (EET). Before EET, the diagonal peaks comprise positive GSB and SE signals, while the RE signal fully cancels GSB at the **21** and **12** CP positions. After EET, the RE pathway cancels GSB at the higher diagonal peak **2**, and the SE signal shifts to **21** CP. The most important Feynman diagrams for the diagonal peak **2** and the cross-peak **21**, before and after EET, are on the right.

Figure 7 shows the illustrative 2D spectra of a weakly coupled system for two cases, before ($t_2$=0) and after ($t_2$>0) EET. Before EET, the 2D spectrum is composed of only diagonal peaks. The signals in these peaks rise from GSB and SE contributions (see $t_2$=0 Feynman diagrams for peak 2). The GSB signals at the cross-peak positions are also present; however, they are completely cancelled out by the RE pathways. For clarity, only population signals are discussed in this section, and ESA pathways to two-exciton states are omitted.

The RE pathways here describe the events where the first two laser pulses interact with one molecule of the weakly coupled dimer, yet the third interaction and the signal comes from a different molecule. With only one interaction from the right (see Fig. 7), the RE contributions carry a negative sign. In addition, the intensities of various signals are scaled with the strengths of the four transition dipole moments involved and shown in the Feynman diagrams (see Fig. 7), the so-called *pre-factors*. For diagonal peaks **1** and **2**, the pre-factors are simply $|\mu_1|^4$ and $|\mu_2|^4$. For the cross-peaks, it is $|\mu_2|^2|\mu_1|^2$ for **21** and $|\mu_1|^2|\mu_2|^2$ for **12**. It is now apparent that at $t_2$=0 time, GSB and RE signals in the CP positions rise with the same pre-factors defining signal strengths, yet opposite signs, leading to the complete cancellation of two contributions.

After downhill EET ($e_2 \rightarrow e_1$), the SE signal from the diagonal peak **2** down-shifts to the **21** CP, as emission is now recorded from $e_1$ energy state instead of $e_2$ (see Feynman diagrams for $t_2>0$ in Fig. 7). Similarly, the RE signal from **21** CP up-shifts to diagonal peak **2**. Therefore, after EET, this RE signal now fully cancels the GSB signal at the higher diagonal peak **2**. The GSB and SE signals at the lower diagonal peak **1** and cross-peak **21** stay constant until molecular relaxation begins.

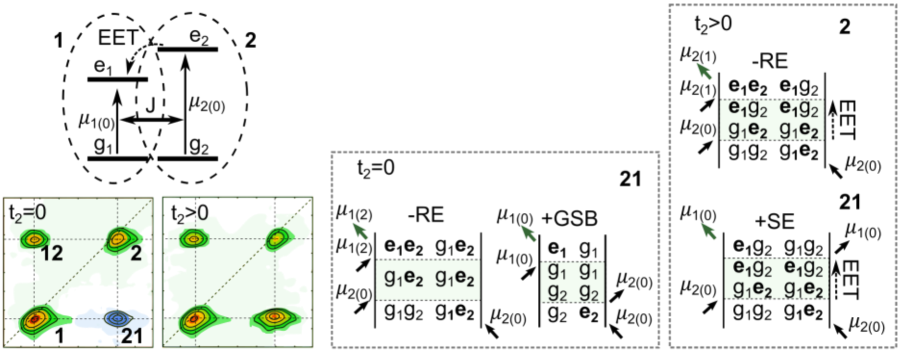

**Figure 8. 2DES of a strongly coupled dimer**

Scheme of energy states for a strongly coupled heterodimer together with two 2D spectra before ($t_2 = 0$) and after ($t_2 > 0$) excitation energy transfer (EET). All the notations are the same as in Fig. 7; just the transition dipole moment of one molecule now depends on the state of its dimeric partner.

The picture is different for the strongly coupled dimer (Fig. 8). The coupling strength ($J$) and the difference between two energy states ($e_2 - e_1$) play an important role in transforming energy states and transition dipoles of the interacting system. The whole interplay was discussed in detail in ref. [102], but the key message is that one molecule's transition now depends on its dimeric partner's molecular state. I.e., transition dipoles, when both molecules are in the ground state ($\mu_{1(0)}$, $\mu_{2(0)}$), are no longer equal to the transition dipoles, when their dimeric partners are in the excited state: $\mu_{1(0)} \neq \mu_{1(2)}$ and $\mu_{2(0)} \neq \mu_{2(1)}$ (index number in the brackets indicates if and which molecule was previously excited). This determines that the pre-factors for the GSB and RE signals in CP positions at early times are no longer equal: $|\mu_{1(0)}|^2|\mu_{2(0)}|^2 \neq |\mu_{1(0)}|^2|\mu_{2(1)}|^2$ for **12** and $|\mu_{2(0)}|^2|\mu_{1(0)}|^2 \neq |\mu_{2(0)}|^2|\mu_{1(2)}|^2$ for **21**. The two signals do not cancel each other but instead result in one positive and one negative CP, as discussed in ref. [102] and showed in the $t_2$=0 2D spectrum in Fig. 8.

Again, after EET ($t_2$>0), signals from the **2** and **21** positions redistribute. SE is now visible from the lower diagonal CP **21**, and RE from the **21** CP position shifts to the higher diagonal peak **2**. However, even though RE and GSB signals overlap, they do not entirely cancel out, as pre-factors for two signals are not equal: $|\mu_{2(0)}|^2|\mu_{2(0)}|^2 \neq |\mu_{2(0)}|^2|\mu_{2(1)}|^2$.

The realistic systems studied with 2DES are much more complicated than the idealistic dimer cases presented in this section. It is rare for all ESA signals to be absent. However, described dynamics of the signals during EET and the presence of the cross-peaks for excitonically coupled systems persist and hold for any TFWM experiment.

# Experimental nuances

The goal of TFWM experiments is to measure the system's third-order response function (signal) with respect to the delay times between the laser pulses, $S^{(3)}(t_3, t_2, t_1)$. For this reason, the experimental setup must generate three ultrashort laser pulses (four for heterodyne detection) and provide a way to change the delays between them. Details about the 2DES setup used for the experiments presented in this thesis can be found in references [106,107] and are discussed briefly in the upcoming section. After introducing the setup, the following two sections describe polarisation control and the global analysis procedure.

## Experimental setup

The 2DES lab in the Division of Chemical Physics, Lund University, is equipped with a PHAROS amplified laser system (Light Conversion Ltd), producing ~200 fs duration laser pulses of 1028 nm fundamental radiation at 200 kHz repetition rate (adjustable by pulse-picker) and the average output power of 6 W. The laser system pumps a lab-built non-collinear optical parametric amplifier (NOPA), which operates as a tuneable light source, providing ultrashort laser pulses (10-20 fs after compression using a prism compressor or a combination of the prism compressor and chirped mirrors) in the visible and near-infrared region (470-950 nm).

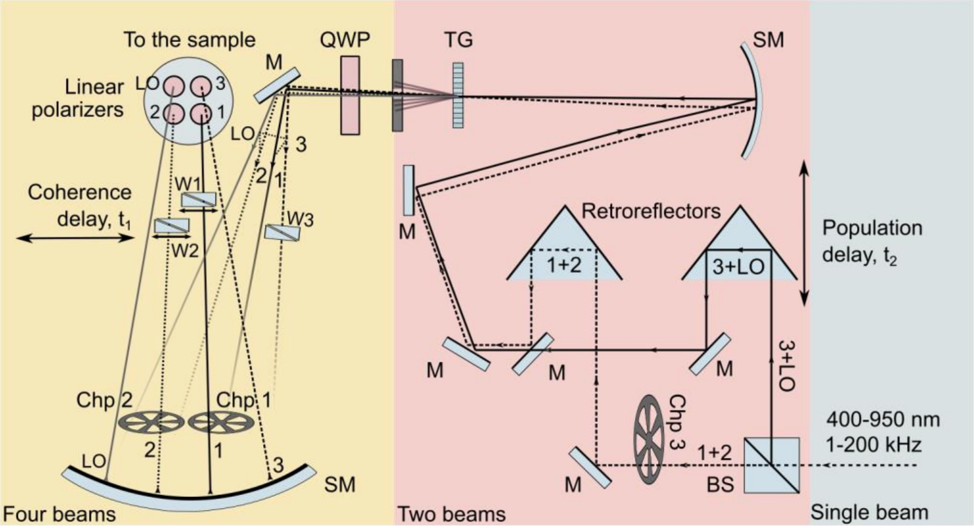

**Figure 9. 2DES experimental setup.**
Experimental setup used for 2DES experiments. The details are presented in the main text and found in ref. [106,107]. Abbreviations used in the picture are: BS – beamsplitter, M – mirror, 1, 2, 3 – numbering of three laser pulses, LO – a fourth pulse, the local oscillator, SM – spherical mirror, TG – transmission grating, QWP – quarter waveplate, Chp – optomechanical chopper, W1, W2, W3 – wedges.

The 2DES experimental setup is presented in Fig. 9. The output of the NOPA is separated into two beams (1+2 and 3+LO, marked with notations of the four future pulses) using a 50/50 broadband beamsplitter (BS). Both beams hit separate retroreflectors, where the population delay ($t_2$) up to 1 ns for the beam 3+LO is implemented using a mechanical delay stage. A spherical mirror (SM) then focuses two beams on a transmission grating (TG), optimised for the $\pm 1^{\mathrm{st}}$ diffraction order. The zero and higher diffraction orders are filtered with masks, and only four pulses, already in a box-CARS geometry, travel further. Linear polarisation of the beams is converted to circular with the broadband quarter waveplate (QWP), and then four beams reflect from the second SM, which focuses them on the sample. Before reaching the sample spot, beams 1 and 2 travel through the fused silica wedges (W1 and W2) to control the coherence delay with a femtosecond time accuracy. The same, but not movable, wedge pair is inserted into beam 3 (W3) to get the same dispersion and delay as beams 1 and 2. Polarisations of individual beams are manipulated by placing four separate linear wire grid polarisers in the path of each pulse just before they reach the sample. Lastly, optomechanical choppers stand in the way of pulses 1 and 2 for double lock-in detection.[106] Modulation of two pulses at two different frequencies allows signal detection at the sum and difference of those frequencies, minimising unwanted contributions from the scattered light.[106] The third chopper, marked as Cph 3, stands in the way of pulse 1+2 and is there for conducting pump-probe experiments.

The experimental setup, as described in Fig. 9, has many advantages. First, it allows manipulation (chop, delay, change polarisation, etc.) of each beam separately. It is also straightforward to measure both rephasing and non-rephasing signals by simply changing the time order between pulses 1 and 2. For this reason, movable wedges stand in the optical paths of both beams (see Fig. 9). Also, the co-propagation of all beams assures phase stability. The beam pairs with required highly accurate time delays (1+2 and 3+LO) always travel together and hit either the same reflective optical element (mirror, retroreflector, etc.) or the same/different transmission element (grating, quarter waveplate, wedges). In this case, if the mirror moves, the relative phase drift between the pulses is the same, and the relative time delay is unaffected. The transmission elements do not introduce this phase drift, as the beam travels through the optics and is mostly immune to its movements.

Implementing the heterodyne detection scheme in a box-CARS geometry amplifies the signal (by mixing it with an LO pulse and recording interferograms between two fields) and minimises the background from the other pump/probe pulses. To eliminate LO contribution in the measured heterodyned signal and to avoid the fourth pulse acting as a probe, the LO is usually delayed from the emitted signal by a fixed time delay. This delay time must be optimised to have as many interference fringes on the detector as possible. However, the pattern should still be well resolved on the spectrometer to measure the signal correctly. In our case, LO is delayed by 2.57 ps.

## Polarisation control

Polarisation control is an important tool to disentangle the nature of transitions, couplings and coherent signals in 2DES.[96,104] For the full polarisation manipulation, individual control of each pulse is necessary – the feature available 'freely' when measuring in the box-CARS geometry. The most commonly used and explored polarisation sequences in 2DES are all-parallel (AP, $\langle 0°, 0°, 0°, 0° \rangle$), magic angle (MA, $\langle 54.7°, 54.7°, 0°, 0° \rangle$) and double-crossed (DC, $\langle 45°, -45°, 90°, 0° \rangle$).

Polarisation control is discussed extensively in Chapter 5 of ref.[88]. Here, only a final result will be presented – the dependency of signal intensities as a function of angles between transition dipole moments and polarisation of four laser pulses (Fig. 11). It is essential to mention, that these results were obtained under some highly restrictive assumptions, e.g. that the magnitudes of dipoles and fields are unity and that the transition dipoles are independent of time. In addition, the ratios of various signals are presented for isotropic samples averaged over all possible molecular orientations. The results are compared with signal intensity for a diagonal peak for an anisotropic sample measured with an AP polarisation sequence. In that case, all molecules are arranged parallel to the laser pulses, so the signal intensity is maximal, $S_{diag}^{anis} = 1$.

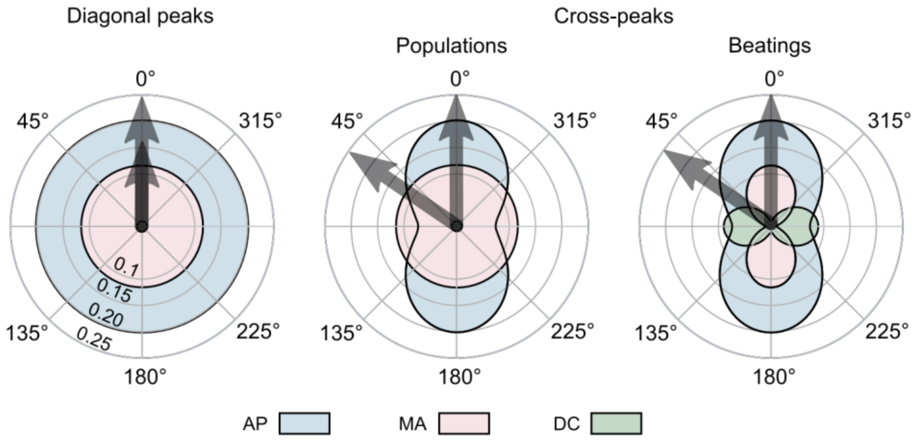

**Figure 10. The ratio of various signal intensities in 2DES with polarisation control**
Ratios between relative intensities of diagonal peaks and cross-peaks for all-parallel (AP, $\langle 0°, 0°, 0°, 0° \rangle$), magic angle (MA, $\langle 54.7°, 54.7°, 0°, 0° \rangle$) and double-crossed (DC, $\langle 45°, -45°, 90°, 0° \rangle$) polarisation sequences. The radial angle shows the angle between dipole moments of two transitions for cross-peaks (this angle is zero for diagonal peaks), and the radius corresponds to the relative intensities. The values are presented relative to the intensity of diagonal peaks for an anisotropic sample and AP polarisation sequence: $S_{diag}^{anis} = 1$.

In Fig. 10, the signals are divided into diagonal peaks, cross-peaks from population signals (couplings and energy transfer) and cross-peaks from beating signals (coherences between two levels). Intensities of diagonal peaks depend only on the polarisation of the pulses since there is only one transition dipole moment involved:

$$S_{diag} = 1/15 \times (\cos\Theta_{12}\cos\Theta_{34} + \cos\Theta_{13}\cos\Theta_{24} + \cos\Theta_{14}\cos\Theta_{23}). \tag{11}$$

Here, the $\Theta_{ij}$ are the angles between polarisations of corresponding laser pulses, e.g. for AP measurements $\Theta_{ij} = 0, \forall\, i, j$. The ratios of signal intensities for the diagonal peaks are $S_{diag}^{AP} = 0.2$ for AP, $S_{diag}^{MA} \approx 0.11$ for MA and $S_{diag}^{DC} = 0$ for DC polarisation sequences.

The intensity ratio for the population signals at the position of CP depends on an angle between the transition dipole moments ($\psi$) and angles between the polarisations of laser fields. For example, population signals in the AP polarisation have the angular dependency of $S_{CP,Pop}^{AP} = \frac{1}{15}(1 + 2\cos^2\psi)$, as visualised in the middle graph of Fig. 10. The MA polarisation sequence now reveals its full potential as the signal intensity of population CP is almost independent of the angle between two transitions. Therefore, the MA polarisation sequence is usually preferred when measuring population transfer signals, to avoid any depolarisation dynamics. For the DC polarisation sequence, the populations signal intensities are again zero: $S_{CP,Pop}^{DC} = 0$.

Finally, when it comes to the beating signals in the cross-peaks, AP and MA polarisations favour signals rising from two parallel transitions, and suppression is visible for signals from two perpendicular ones (right graph in Fig. 10). However, signals from two transitions with transition dipole moments that are at the right angle in DC polarisation are not zero anymore. Therefore, the DC polarisation sequence $\langle 45°, -45°, 90°, 0° \rangle$ suppresses all signals from single electronic states (populations or vibrational coherences) while leaving out only signals involving two electronic transitions (electronic coherences or coherences excited via vibronically coupled transitions). For this reason, a general and extremely useful practice when measuring and analysing coherences in 2DES is to compare beating signals from AP and DC measurements.[104,108,109]

## Global analysis procedure

The global analysis procedure provides characteristic time constants of the photo-induced processes in 2DES experiments.[110,111] The population kinetics and oscillations (quantum beatings) in each point of the 2D spectrum are fitted in conjunction with dynamics from the other points as a sum of exponential decays/rises and damped oscillatory signals (Fig. 11).

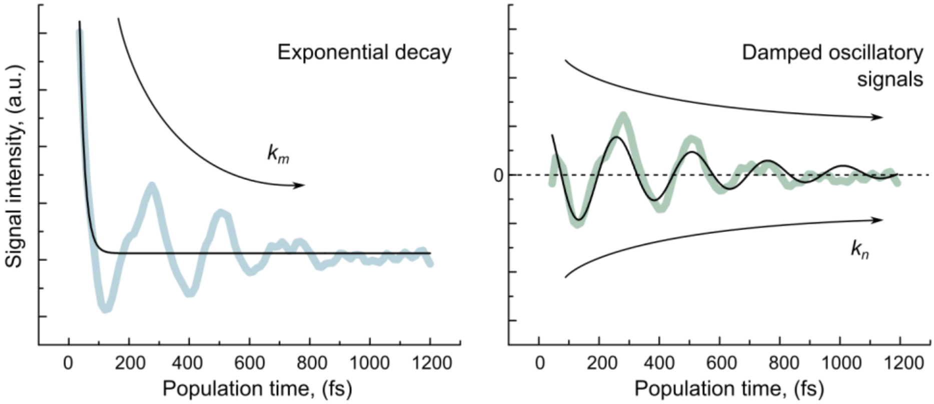

**Figure 11. Single point kinetics in 2DES**
The temporal evolution of a single point kinetics in 2D spectra often displays two different types of dynamics – multi-exponential decay/rise (population transfer) and damped oscillatory features (coherences or quantum beatings).

The global fitting equation for each point of the 2D spectrum $(\tilde{\nu}_1, \tilde{\nu}_3)$ can be written as the following expression:

$$S^{(3)}(\tilde{\nu}_1, t_2, \tilde{\nu}_3) = \sum_m A_m^{DAS}(\tilde{\nu}_1, \tilde{\nu}_3) e^{-k_m t_2} + \sum_n A_n^{OM}(\tilde{\nu}_1, \tilde{\nu}_3) e^{-k_n t_2 - i(\tilde{\nu}_n t_2 + \varphi_n)}. \quad (12)$$

Here, $A$s are the initial amplitudes, $k$s – rate constants, proportional to decay times ($k_{m,n} \sim {}^{1}/_{t_{m,n}}$), $\tilde{\nu}_n, \varphi_n$ – frequencies and phases of oscillatory signals (QB). Indices $m$ and $n$ represent the number of fitted exponential and oscillating components, respectively. For every exponential decay rate, $k_m$, 2D decay associated spectra (DAS) can be plotted using the fitted amplitudes, $A_m^{DAS}(\tilde{\nu}_1, \tilde{\nu}_3)$. The same can be done for each fitted frequency, $\tilde{\nu}_n$, where fitted amplitudes, $A_n^{OM}(\tilde{\nu}_1, \tilde{\nu}_3)$, build a so-called oscillation map (OM). A detailed explanation of our global analysis approach and composition of DAS/OM can be found elsewhere.[110,111]

Figure 12 presents conventional 2D DAS for EET between two electronic states and OM for vibrational beatings. The DAS indicates the downhill EET from $e_2$ to $e_1$ state. To explain the apparent signals in a simple way, positive peaks in DAS show a diminishing signal intensity of the positive signal in the 2D spectrum (e.g. energy leaving the state). In contrast, negative signals correspond to an increase in positive signal intensity (e.g. energy arriving at the particular state). The signs in DAS are opposite for the negative spectral features. The fitted decay/rise time of each DAS ($t_m \sim {}^{1}/_{k_m}$) indicates the observed rates of the involved processes. The characteristic OM of $\tilde{\nu}_2$ wavenumber vibrational beatings in the rephasing part of the signal is presented on the right side in Fig. 12. After the fitted DAS are subtracted from experimental data, the characteristic frequencies can be obtained by performing a real FT or complex FT over the signal residues. The complex FT can discriminate between signals evolving with either $e^{+i\tilde{\nu}_2 t_2}$ or $e^{-i\tilde{\nu}_2 t_2}$ phases, while the result from the real FT (as in Fig. 12) combines features from both signals. In connection with double-sided Feynman diagrams, positive $\tilde{\nu}_2$ frequencies originate from $|2\rangle\langle 1|$ coherences during the $t_2$ time period and negative frequencies from $|1\rangle\langle 2|$ superposition. Here, numbers 1 and 2 mark states of the system, which can be of any origin (ground or excited electronic, vibrational or vibronic) with a valid energy inequality of $2 > 1$.

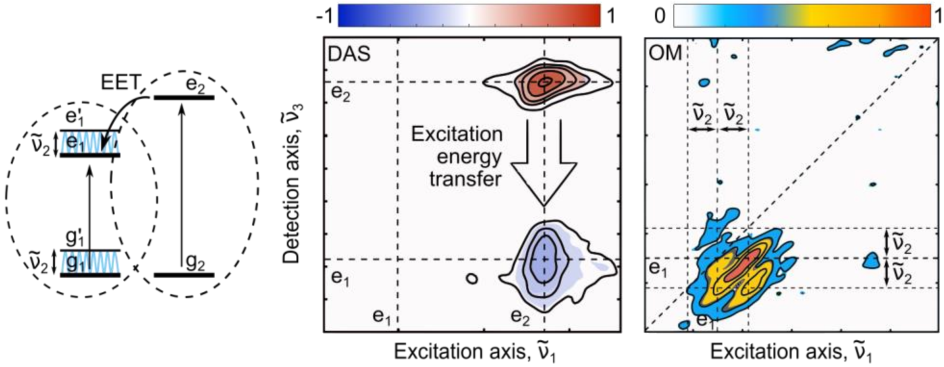

**Figure 12. Illustrative DAS and OM**

Energy scheme for a weakly coupled heterodimer with indicated electronic ground ($g_1,\ g_2$) and excited ($e_1,\ e_2$) states, and vibrational levels ($g_1'$, $e_1'$, where $g_1' - g_1 = e_1' - e_1 = \tilde{\nu}_2$). Conventional decay associated spectrum (DAS) represents EET (excitation energy transfer) between the states ($e_2 \rightarrow e_1$). The positive peak indicates population decrease, and the negative peak indicates population growth in a particular state. Also presented is a characteristic oscillation map (OM) for vibrational beatings with $\pm\tilde{\nu}_2$ wavenumbers, as observed in the rephasing part of the signal.

Performing the complex FT on the rephasing part of the signal is highly advantageous, as the procedure can help distinguish between the ground and excited state coherences. As presented in detail in Supplementary information of ref. [104], positive frequencies in the rephasing part of the signal can only originate from the excited state, while negative frequencies can come from coherences either in the ground or in the excited states. In addition, purely electronic beatings have the same amplitudes for positive and negative frequencies, while for vibrational coherences, amplitudes of QB with negative wavenumbers usually dominate the OM.

The vibrational, electronic or vibronic beatings result in specific peak patterns in OM and thus can be used when defining the origin of coherences.[96,97] However, it is essential to remember that these patterns might be altered depending on the laser spectrum coverage of the involved transitions.[109] In addition to specific OM, the lifetimes of electronic beatings (dephasing) are usually much shorter in molecular systems than the lifetimes of vibrational/vibronic beatings (hundreds of femtoseconds compared to lifetimes close to or longer than a picosecond for electronic and vibrational coherences, respectively).[103,104,109] With the help of this knowledge, the origin of oscillations and even the nature of involved states can be determined quite accurately.

# Main results

This chapter will summarise the main results of the included published papers and manuscripts. The experimental observation of vibronic coupling in a photosynthetic pigment – chlorophyll *c1* – was demonstrated in Paper I. The dynamic band-shift signals in 2DES were characterised in Paper II. The obtained knowledge was then used to track charge separation in reaction centres of purple bacteria $\mathrm{bRC}_{\mathrm{sph}}$ and green bacteria $\mathrm{bRC}_{\mathrm{cfx}}$, as presented in Papers III and IV. Papers III and IV also introduce the first identification of a low-lying initial charge-transfer state within the special pair in both reaction centres. Lastly, energy transfer and trapping in the photosynthetic units of intact living cells of the green bacteria *Chloroflexus aurantiacus* were presented in Paper V.

## Vibronic coupling in chlorophyll-type molecules

The vibronic coupling between the $Q_y$ and $Q_x$ states in Chl *c1* molecule was explored with polarisation-controlled 2DES at 77 K, and the findings were presented in Paper I. The Chl *c1* was extracted from light-harvesting complexes of the diatom *Cyclotella meneghiniana*.[112] Although not a very common Chl-type molecule, Chl *c1* made a great candidate to observe vibronic coupling, as the two visible transitions were nearby energetically (~1000 $\mathrm{cm}^{-1}$) and almost equal in intensity (see Fig. 13(a)).

The two 2D spectra at $t_2$=100 fs population times from two sets of experiments: an all-parallel polarisation arrangement (⟨0°,0°,0°,0°⟩, AP) and a double-crossed (⟨45°,-45°,90°,0°⟩, DC), are presented in Fig. 13(b). From the global analysis of AP data, the EET between Q states ($Q_x \rightarrow Q_y$) was found to be rapid and happened on the 100 fs timescale.[113,114]

Figure 14 summarises the main findings from the 2DES DC data analysis. As presented in the subchapter "Polarisation control", only beating signals between two transitions with a non-parallel orientation survive in DC polarisation measurements. These beatings can originate from either electronic coherences or coherences excited via vibronically coupled transitions. In addition, the QB with *positive* wavenumbers in the rephasing part of the signal indicates the presence of excited state coherences, while the *negative* wavenumbers below the diagonal could indicate both excited and ground state coherences.[103] To exploit this feature, a separate complex FT analysis of above and below diagonal signals was performed. The fitted regions are indicated by the dashed rectangles in the 2D spectra in Fig. 13(b).

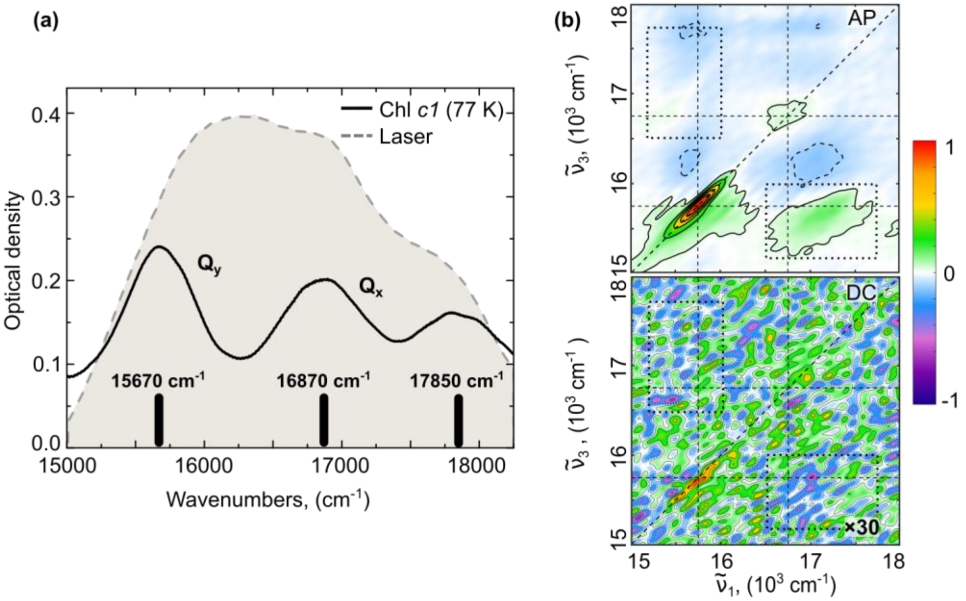

**Figure 13. 2DES of Chl *c1* molecule**

Low temperature (77 K) absorption spectrum of Chl *c1* (solid black line) overlayed with laser spectrum (shaded area) used in 2DES experiments (a). Solid vertical bars indicate two main transitions, denoted as $Q_y$ and $Q_x$. The third transition, visible at 17850 cm$^{-1}$, is most likely a band rising from the vibronic coupling between the electronic state $Q_x$ and vibronic levels of $Q_y$.[25] The real (absorptive) component of the total (rephasing+non-rephasing) 2DES data from AP and DC polarisation experiments at $t_2$=100 fs are presented in the (b) part. The DC spectrum is scaled by a factor of 30 to make weak features visible. Contour lines (solid for positive, dashed for negative signals) are spaced by every 20% of the maximum signal, and an additional contour line is drawn at 2.5% to make weak signals more apparent. Dotted rectangles mark the CP areas, integrated to obtain Fourier amplitudes for the beating signals. The figure is adapted from Paper I.

The strongest beating signals in the upper CP region were of +1070 cm$^{-1}$ and +1200 cm$^{-1}$ wavenumbers. Beatings of five frequencies dominated the corresponding lower CP region: -1000 cm$^{-1}$, -1180 cm$^{-1}$, -1230 cm$^{-1}$, -1280 cm$^{-1}$ and -1540 cm$^{-1}$ (see Fig. 14(a)). From the patterns of the signals in OM, intensities of OM for $\pm\tilde{\nu}_2$ frequencies (Fig. 14(b)), and the lifetimes of QB signals, it was concluded that beatings with positive frequencies originated from vibronically coupled excited state transitions and that more than one vibrational mode was engaged in vibronic coupling (see Paper I for details). The below diagonal CP signals were dominated by the vibrational ground state coherences, excited via vibronically coupled transitions in the excited state. The frequencies of these ground state coherences matched the existing vibrations present in the Chl *c* Raman spectrum: 1000 cm$^{-1}$, 1180 cm$^{-1}$, 1240 cm$^{-1}$, 1280 cm$^{-1}$ and 1560 cm$^{-1}$.[115]

Evaluation of the suppression ratio for the signals from AP and DC experiments using vibrational transition of the isopropanol (used solvent) impulsive Raman mode at 810 cm$^{-1}$ suggested a significant suppression ratio of >660 (see SI of Paper I). This ratio was approximately 60 times stronger than the suppression factor for the surviving Chl *c1* signals in DC (~11 for the beatings in the 1200 cm$^{-1}$ region). This fact ensured that visible beatings came from coherences between transitions with non-parallel transition dipole moments and not from signals that leaked through the polarisers. Observing these beatings in the DC polarisation measurements was indisputable proof of vibronic coupling/mixing in the Chl *c1* molecule and is expected to hold true to the rest of the Chl-type molecules.

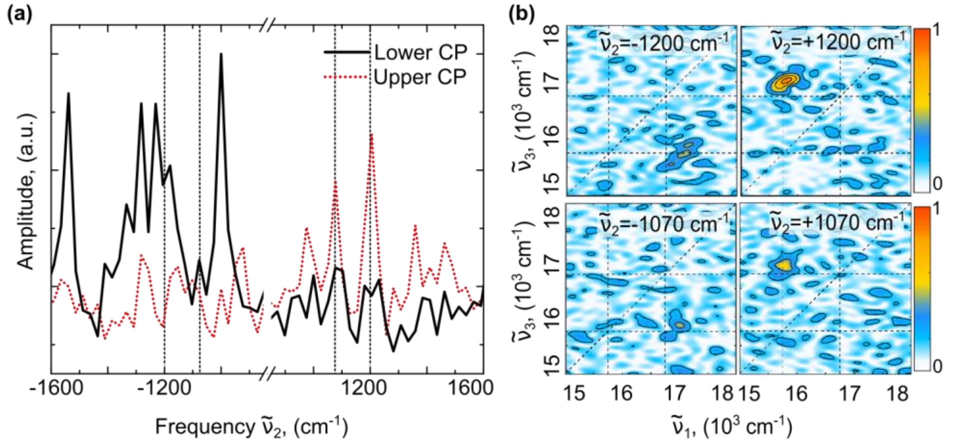

**Figure 14. Analysis of the beating signals in DC 2DES**

(a) Fourier transform amplitude obtained from the cross-peak (CP) regions (lower versus upper) after fitting the rephasing part of the 2DES data with exponential decay/rise kinetics and subtracting the fits from the signal. Vertical dashed lines indicate ±1070 cm$^{-1}$ and ±1200 cm$^{-1}$ wavenumbers. Positive and negative $\tilde{\nu}_2$ oscillation maps for two selected wavenumbers are presented in the (b) part. Different intensities between OM for positive and negative frequencies indicate that excited coherences are not of electronic origin. Figure adapted from Paper I.

# Dynamic band-shift signal in bRC

In some systems, like bRCs, light absorption leads to charge separation and an internal electric field formation. In time-resolved spectroscopy, the charge separation can be conveniently tracked via the Stark effect and the formation of a derivative-shaped dynamic band-shift signal.[68,69] Although this signal is well defined and understood in TA measurements,[66,67] its appearance is not so intuitive in 2DES. For this reason, the dynamic band-shift signal and intrinsic dynamics during the internal charge separation in the bRC$_{\mathrm{sph}}$ system were described and characterised in Paper II.

Figure 15(a) presents schematics of the transient Stark effect in quinone-reduced bRC$_{\mathrm{sph}}$, where positively charged special pair ($P^+$) and negatively charged BPheo ($H_A^-$) create an internal electric field, $\boldsymbol{E}$. The slices of 2D spectra at the B band excitation region in Fig. 15(b) visualise the two cases before and after charge transfer (CT). The side 1D spectra were obtained after integrating 2D data over the presented excitation ($\tilde{\nu}_1$) region and correspond to the TA-type signals. Horizontal bars mark transitions of two accessory BChl, before ($B_A$ and $B_B$) and after CT ($B_A'$ and $B_B'$). The dynamic band-shift signal – a positive peak changing rapidly to a negative one – forms in the system with the characteristic time of charge separation.

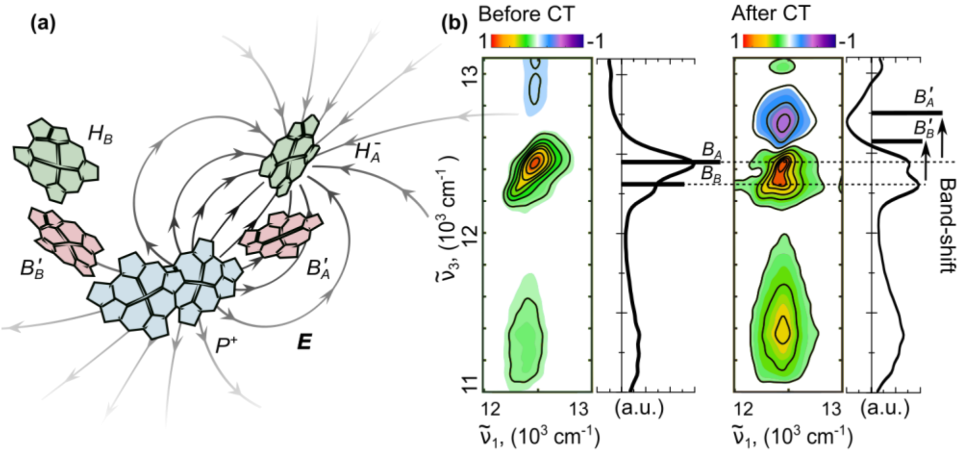

**Figure 15. Stark effect in bRC$_{\mathrm{sph}}$**

Formation of the charge-separated state ($P^+H_A^-$) in purple bacteria bRC$_{\mathrm{sph}}$, observed as a band-shift signal for the co-factors within the internal electric field, $\boldsymbol{E}$. (a) The structure of quinone-depleted bRC$_{\mathrm{sph}}$ from ref. [52] after the formation of charge separated state. Vector lines illustrate the static electric field between positively charged special pair ($P^+$) and negatively charged BPheo ($H_A^-$). (b) The slices of 2D spectra from the B excitation region ($\tilde{\nu}_1$ between 12000-13000 cm$^{-1}$) before and after charge transfer (CT). On the side of each 2D spectrum, the TA-like signal is plotted, obtained after integration over $\tilde{\nu}_1$ axis. Two BChl transitions ($B_A$ and $B_B$) and their shifted states ($B_A'$ and $B_B'$), extracted from the data analysis are marked with solid black bars.

The main findings from Paper II are summarised in Fig. 16. Kinetic traces extracted from six points, as indicated in Fig. 16(a), are presented in Fig. 16(b) with thick grey lines. The data is overlaid with global analysis fits with three time components: 100 fs, 1.7 ps and >1 ns. Time components stood for EET, ET and relaxation processes and were discussed in more detail in Paper II. Negative signals at points (1), (2) and (3) formed with the time of charge transfer (1.7 ps) and were described with RE pathways (see Feynman diagrams in the inside of Fig. 16(b)) to the Stark-shifted BChl transitions ($B_A \rightarrow B'_A$ and $B_B \rightarrow B'_B$). Sudden drops of signal intensities at points (5) and (6) come from extremely fast (100 fs) downhill EET between B→P bands, followed by the recovery of the signal at points (4)-(6). This re-emerging of the signals happens with the time of charge separation (1.7 ps) and stems from the partial exposure of the GSB signals of $B_A$ and $B_B$ transitions.

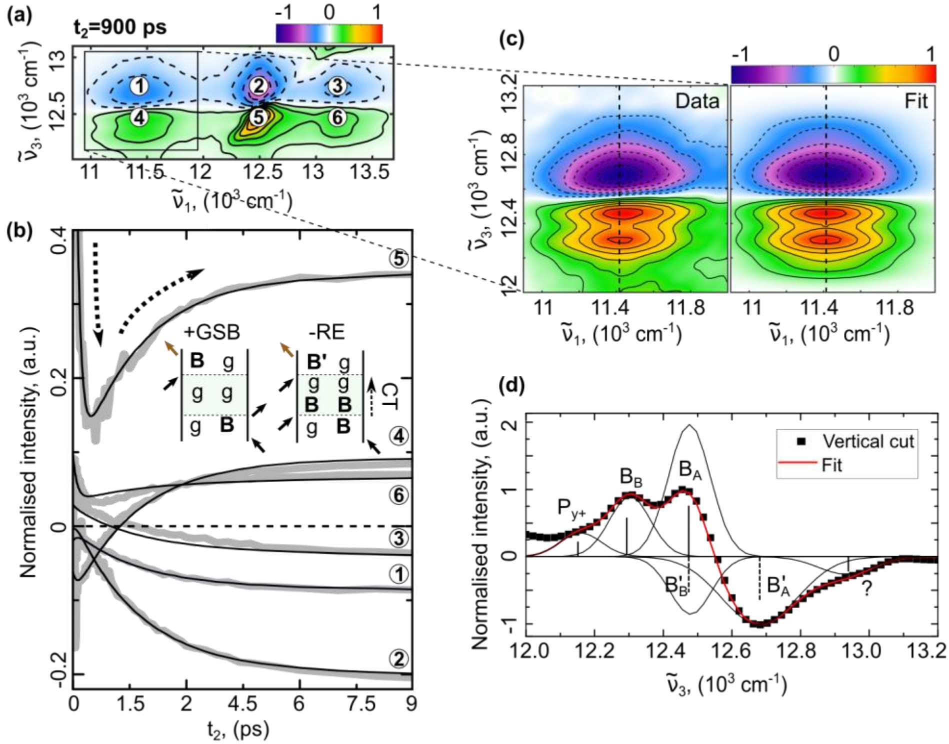

**Figure 16. Dynamic band-shift signal**

Single point kinetics at six points, as indicated in (a), comprising the band-shift signal. Coordinates $(\tilde{\nu}_1, \tilde{\nu}_3)$ in cm$^{-1}$ of the points are as follows: (1) (11440,12700); (2) (12500,12700); (3) (13200,12700); (4) (11440,12450); (5) (12500,12450); (6) (13200,12450). Grey thick lines in the (b) graph show experimental data and thin black lines – multi-exponential fit, with three characteristic times of 100 fs, 1700 fs and >1 ns. On the right, in (c), the band-shift region from $t_2$=900 ps 2D spectrum ("Data") in comparison with a fit of six Gaussian profiles ("Fit"). The (d) graph demonstrates vertical cuts at $\tilde{\nu}_1$=11420 cm$^{-1}$; the squares correspond to experimental data and a solid red line – to the fit. The band with a question mark does not have a clear assignment yet. Figure adapted from Paper II.

To estimate the electrochromic shifts of the $B_A$ and $B_B$ transitions for bRC$_{sph}$, the above diagonal CP at $t_2$=900 ps population time was fitted with six Gaussian profiles. The comparison between the measured data and the fit is presented in Fig. 16(c) and (d), and the centres of six Gaussian profiles are summarised in Table 1. The estimated band-shifts for the two accessory bacteriochlorophylls were $\Delta\nu_A$=200 cm$^{-1}$ and $\Delta\nu_B$=180 cm$^{-1}$. In addition, transition at the 12160 cm$^{-1}$

wavenumbers was proposed to be the higher excitonic transition of the special pair $P_{y+}$ as in ref. [116], while the origin of the 12930 cm$^{-1}$ transition could not be exactly determined.

**Table 1. Centres of six Gaussian profiles**

Centres of six Gaussian bands used to fit the band-shift signal, as presented in Fig. 16(c) and (d). Values are in wavelengths (nm) and wavenumbers (cm$^{-1}$).

| $bRC_{sph}$ | $P_{y+}$ | $B_B$ | $B_A$ | $B'_B$ | $B'_A$ | ? |
|---|---|---|---|---|---|---|
| nm | 822 | 813 | 801 | 801 | 788 | 773 |
| cm$^{-1}$ | 12160 | 12300 | 12480 | 12480 | 12680 | 12930 |

# 2DES of bacterial reaction centres

Results from two 2DES experiments of quinone-depleted $bRC_{sph}$ from purple bacteria *Rhodobacter sphaeroides* and quinone-reduced $bRC_{cfx}$ from green bacteria *Chloroflexus aurantiacus* were presented in Papers III and IV. It is only natural to introduce the main findings from the three Papers in parallel, as they strongly relate to each other, and some of the conclusions about $bRC_{cfx}$ are drawn from the (assumed) structural similarities to the $bRC_{sph}$ complex.

## Low temperature absorption spectra

Linear absorption spectra (black dots) of quinone-depleted $bRC_{sph}$ (a) and quinone-reduced $bRC_{cfx}$ (b) in the visible and near-infrared region at cryogenic temperature (77 K) are presented in Fig. 17. The absorption spectrum of $bRC_{sph}$ consists of three main bands: **H** at 760 nm, **B** at 803 nm and **P** at 880 nm. In the $bRC_{cfx}$ case, the bands are located at 757 nm (**H**), 813 nm (**B**) and 890 nm (**P**). In addition to three major peaks, the $bRC_{cfx}$ absorption spectrum has a visible shoulder transition at 794 nm. Seven Gaussian profiles (shaded curves) stand for the transitions of the co-factors, and the centres of the bands are listed in Table 2. Shadings of the Gaussian peaks correspond to the selected colours of co-factors in the respective bRC structures. The cumulative fits of the spectra with eight Gaussian profiles are depicted with thin red lines. An additional, extremely broad Gaussian band was necessary for both fits to converge (visualised with unshaded curves in Fig. 17).

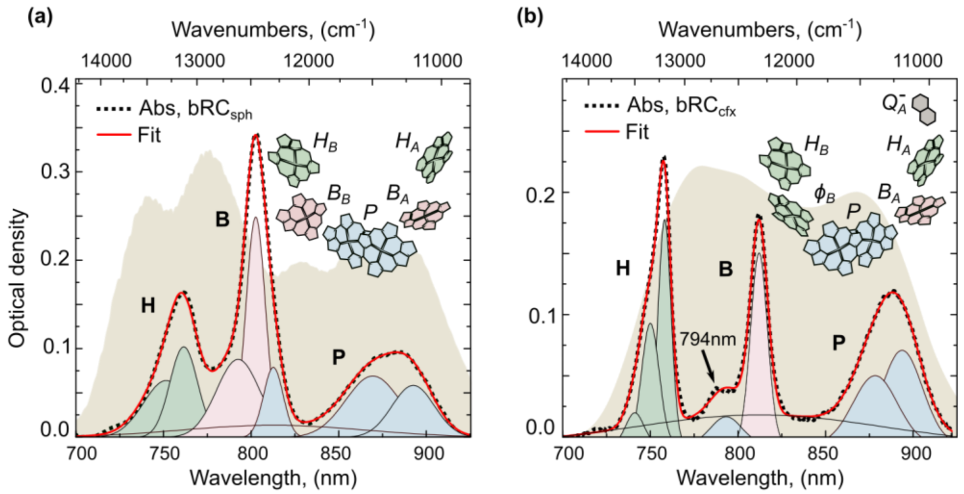

**Figure 17. Absorption spectra and structures of bRC$_{sph}$ and bRC$_{cfx}$**
Low temperature (77 K) absorption spectra of bRC$_{sph}$ (a) and bRC$_{cfx}$ (b) in black dots overlaid with the cumulative fits (red, solid lines) using eight Gaussian profiles. The insides of the graphs present the structure of quinone-depleted bRC$_{sph}$, as determined from X-ray crystallography,[52] and a tentative structure of quinone-reduced bRC$_{cfx}$, adapted from bRC$_{sph}$ data. Colour coding of the seven Gaussians corresponds to transitions of different pigments in the systems. Adding one rather broad Gaussian was necessary for both fits to converge.

**Table 2. Centres of seven Gaussian bands**
Centres of seven Gaussian bands used to fit absorption spectra at 77 K for two bRCs. Values are presented in wavelengths (nm) and wavenumbers (cm$^{-1}$).

| | | | | | | | |
|---|---|---|---|---|---|---|---|
| ***Rhodobacter sphaeroides*** **(bRC$_{sph}$)** | | | | | | | |
| nm | 750 | 760 | 790 | 802 | 813 | 870 | 892 |
| cm$^{-1}$ | 13330 | 13160 | 12660 | 12470 | 12300 | 11500 | 11210 |
| ***Chloroflexus aurantiacus*** **(bRC$_{cfx}$)** | | | | | | | |
| nm | 740 | 750 | 760 | 794 | 813 | 880 | 896 |
| cm$^{-1}$ | 13510 | 13330 | 13160 | 12600 | 12300 | 11360 | 11160 |

As visible from the fits, in the bRC$_{sph}$ case, two BPheo transitions lie under the **H** band, and two accessory BChl molecules form the strongly absorbing **B** band. The red side of the **B** band also covers the higher excitonic state, $P_{y+}$. In the bRC$_{cfx}$ case, the accessory BPheo ($\phi_B$) contributes to the absorption increase of the **H** band, so the **B** band rises solely from a single Q$_y$ transition of the $B_A$ co-factor.[54] The **P** bands in both cases are composed of a lower excitonic transition of the special pair dimer ($P_{y-}$) and a charge transfer state ($P_{CT}$). For bRC$_{sph}$, the higher excitonic state, $P_{y+}$, was determined to be at 822 nm (12160 cm$^{-1}$); see Paper II for the details. For the bRC$_{cfx}$ system, the $P_{y+}$ state appears as a small shoulder band at 794 nm (12600 cm$^{-1}$), as was indicated in Paper IV.

## Excitation energy and electron transfer timescales

Rates of excitation energy and electron transfer in $bRC_{sph}$ and $bRC_{cfx}$ were obtained from the global analysis procedure of low temperature (77 K) AP 2DES data. Representative 2D spectra for both complexes at three different population times are depicted in Fig. 18. As mentioned before, global analysis of 2DES data from the quinone-depleted $bRC_{sph}$ provided three characteristic time constants: 100 fs for EET, 1.7 ps for ET and >1 ns for relaxation back to the ground state (Paper II). The times were in good agreement with the already reported values.[70,73,74] The exact **B→P** and **H→B→P** EET time steps were not detected, most probably because kinetics from the first 80 fs were removed from our data analysis to avoid the pulse overlap effects.[117]

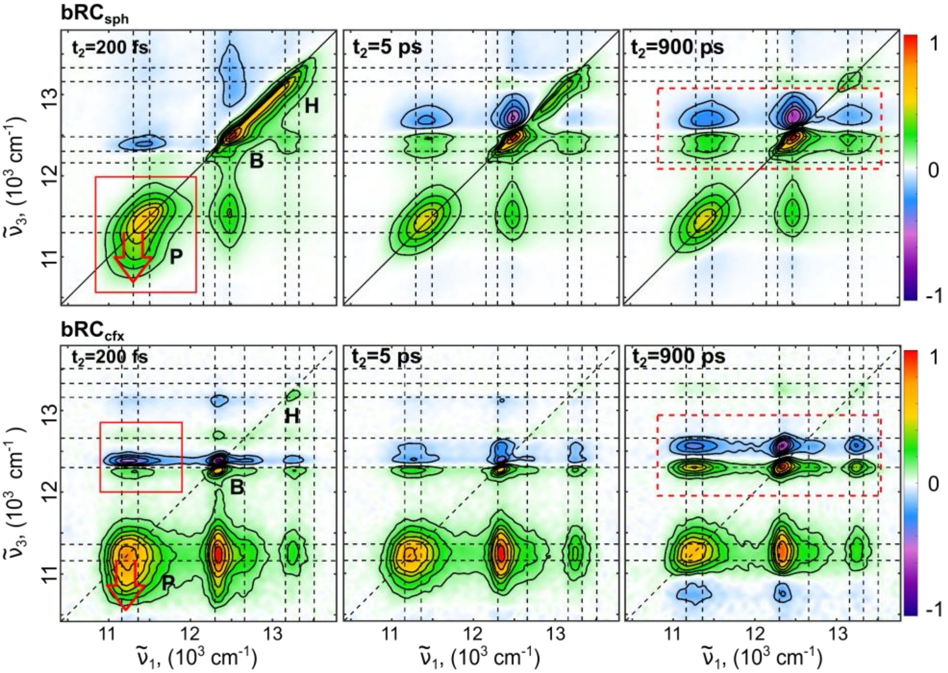

**Figure 18. 2D spectra of $bRC_{sph}$ and $bRC_{cfx}$**

Normalised total absorptive 2D AP spectra of $bRC_{sph}$ (top) and $bRC_{cfx}$ (bottom) at 77 K. Diagonal peaks correspond to three main bands (**P**, **B** and **H**) as visible in the absorption spectra (Fig. 17), and kinetics in the below diagonal peaks indicate downhill EET. Solid-line rectangles in $t_2$=200 fs spectra indicate regions used for tracing internal CT states, as presented in Fig. 19. The swift Stoke shift is marked with red down arrows in $t_2$=200 fs spectra, and dynamic band-shift signals rising after the formation of the $P^+H_A^-$ state is specified with red dashed rectangles in $t_2$=900 ps for both bRCs.

Analysis of quinone-reduced $bRC_{cfx}$ 2DES data resulted in six time components: 15 fs, 85 fs, 250 fs, 4.2 ps, 69 ps, and >1 ns (Paper IV). The shortest time component (15 fs) indicated an extremely fast Stoke shift from the excited $P^*$ state and the formation of the *minor* band-shift signal ($\Delta\nu_{min} = 70\ \text{cm}^{-1}$). The 85 fs and 250 fs time components (previously unreported) corresponded to **B→P** and **H→B→P** EET, respectively. The time constants of 4.2 ps and 69 ps showed bi-exponential ET and formation of $P^{+}H_{A}^{-}$, as indicated by the *major* band-shift signal ($\Delta\nu_{maj} = 270\ \text{cm}^{-1}$) (see Paper IV for details). The two CT times for the quinone-reduced system were slower than for the previously reported quinone-depleted systems, most likely because the reaction centre was in a *closed* state, with a negative charge on $Q_{A}^{-}$.[118] Lastly, one of the conclusions of Paper IV was that bi-exponential CT dynamics originated from two different conformational states of the sample, as previously suggested in ref. [77].

## Identification of charge transfer states

First ideas about the presence of two states under the **P** band for various bRCs were introduced in the early 80s.[79–82] In the discussions, one state was always assumed to be the lower excitonic state of the special pair dimer ($P_{y-}$), while the origin of the second state was hotly debated. One possible suggestion was that it is a low-lying charge-transfer (CT) state, $P_{CT}$;[79] however, the final consensus was that dual structure comes from a structural inhomogeneity within the sample.[84] Just recently, the question was revisited by Yakovlev and Shuvalov,[119] as oscillating signals under the **P** band of bRC$_{\text{cfx}}$ were explained with the possible presence of two separate states, the excitonic state ($P_{y-}$) and the CT state ($P_{CT}$). Our studies in Papers III and IV provide the first unambiguous time-resolved spectroscopy observations of initial charge transfer states under the **P** band in both bRC$_{\text{sph}}$ and bRC$_{\text{cfx}}$ systems.

A significant number of studies introduced general characteristics of the CT states, such as large and fast Stoke shifts;[120,121] large permanent dipole moments;[69,122] and possible mixing with and altering properties of other molecular transitions.[120,123] The findings in Paper III and IV revealed various ways to observe the formation of the internal CT state using time-resolved spectroscopy. The main results from these studies are summarised in Fig. 19.

For bRC$_{\text{sph}}$ (Fig. 19, (a)), the essential indication of the separate CT state was a Stokes shift happening only from the lower-energy part of the **P** band. The SE signal from the Stokes-shifted state disappeared with the characteristic time of electron transfer, as apparent from the exact overlap between the SE from the Stokes-shifted state and the contour lines of the 1.7 ps DAS indicating charge transfer. This led to the conclusion that the state undergoing the Stokes shift was an initial state to the charge separation.

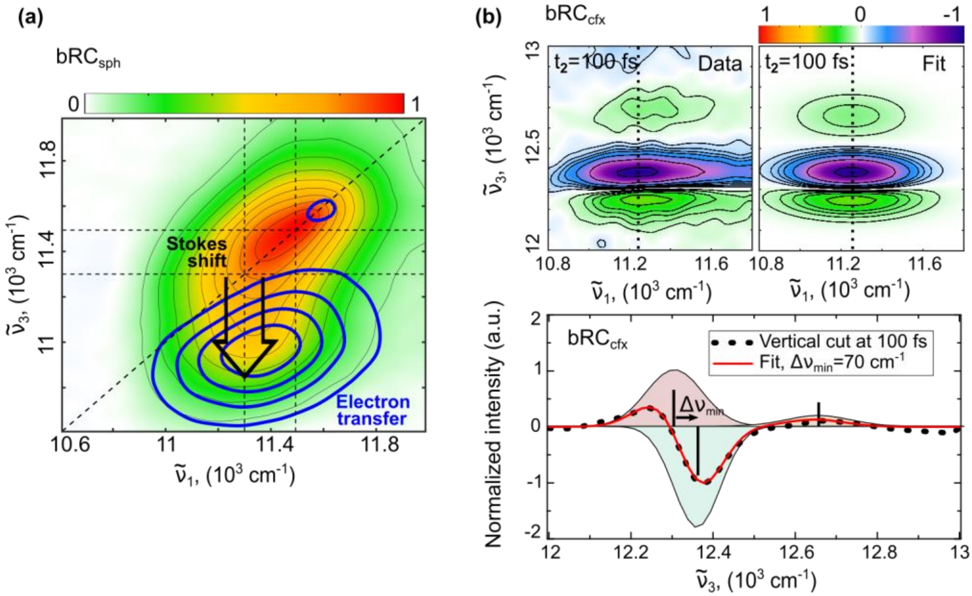

**Figure 19. Observations of charge transfer states**

(a) The observation of the CT state in the bRC$_{sph}$ system. The figure combines the $t_2$=180 fs 2D spectrum (in colours) and 1.7 ps DAS component for ET (thick contour lines). Matching signals indicate that SE from the Stokes-shifted $P_{CT}$ state disappeared with the characteristic lifetime of electron transfer. (b) The **PB** CP region from the $t_2$=100 fs 2D spectra of bRC$_{cfx}$ (Data) and the simulated fit (Fit) using three Gaussian profiles. The evaluated *minor* dynamic band-shift signal from the centres of three Gaussian bands was $\Delta\nu_{min}$=70 cm$^{-1}$. The corresponding 2D spectral regions – the **P** band for bRC$_{sph}$ and **PB** CP for bRC$_{cfx}$ were also indicated with solid rectangles in $t_2$=200 fs 2D spectra in Fig.18. Figure adapted from Papers III and IV.

For bRC$_{cfx}$, the presence of the $P_{CT}$ state was discovered by the extremely rapid (or instantaneous) formation of a *minor* band-shift signal (Fig. 19(b)). After direct excitation to the $P$ state, the band-shift signal emerged immediately, together with the Stokes shift of the excited $P^*$ state. The size of this minor dynamic band-shift signal was determined to be $\Delta\nu_{min} = 70\ \text{cm}^{-1}$. It was concluded that this initial state forming in the bRC$_{cfx}$ immediately after excitation had an asymmetric charge distribution and a strong resemblance to the $P^+$ – two specific properties of CT states in bRCs.[124–126] In addition, similarly to the bRC$_{sph}$, SE signals from the Stokes-shifted state disappeared with the characteristic times of electron transfer (see Paper IV for details). After considering all the findings, it was determined that the state forming in bRC$_{cfx}$ was an internal charge transfer state in the special pair dimer involving the immediate environment, functioning as an initial precursor state for ensuing electron transfer.

The initial minor band-shift formation in bRC$_{sph}$ was not detected in our 2DES data. It could be that removal of the initial 80 fs population times due to the pulse overlap effects cut out the responsible signals. In addition, the **B** band in $bRC_{sph}$ is much more congested than in $bRC_{cfx}$ (see Fig. 17), so various signals overlap and obscure each other. However, based on the structural and optical similarities of the two bRCs (and all type II reaction centres in photosynthetic bacteria), the $P_{CT}$ state should be a general feature of the bRCs, serving as a precursor to the electron-transfer process.

## Energy flow and trapping in the living cells of *Cfx. Aurantiacus*

The excitation energy transfer and trapping kinetics were measured in the living cells of *Cfx. Aurantiacus* and the findings were presented in Paper V.

The room temperature absorption spectrum of whole cells is presented in Fig. 20, with a thick black line. Spectral contributions from various photosynthetic units: the chlorosome aggregate and baseplate, the B808-866 complex[127] and $bRC_{cfx}$ are also presented for illustrative purposes. The shaded curve in the background stands for the laser spectrum used in our 2DES experiments. The spectrum was tuned, so it only excited the low-energy part of the chlorosome band. Four representative 2D spectra at various population times, measured at room temperature with the MA polarisation sequence, are also shown in the figure. Prominent diagonal peaks in the early time $t_2$=30 fs 2D spectrum match the main bands of the absorption spectrum. The spectral changes over the population time indicate EET between the sub-units (chlorosome→ baseplate→ B808-866→ bRC) and energy trapping in a charge-separated state ($P^+H_A^-$) inside the photo-active bRC.

To separate the spectral evolution corresponding to the energy and electron transfer, the 2D spectrum was divided into three areas along the excitation axis, and the global analysis procedure was performed for each region separately. Three regions were the B866 ($\tilde{\nu}_1$ between 10600-11900 $cm^{-1}$), the B808 and the baseplate (11900-12900 $cm^{-1}$) and the chlorosome (12900-13300 $cm^{-1}$), as indicated in Fig. 21. The DAS for five main time components, obtained from the certain spectral regions, are also presented in Fig. 21. All DAS were normalised to 1, and the band-shift region of the 27 ps and 110 ps DAS were additionally multiplied by 5, to make the weak features visible.

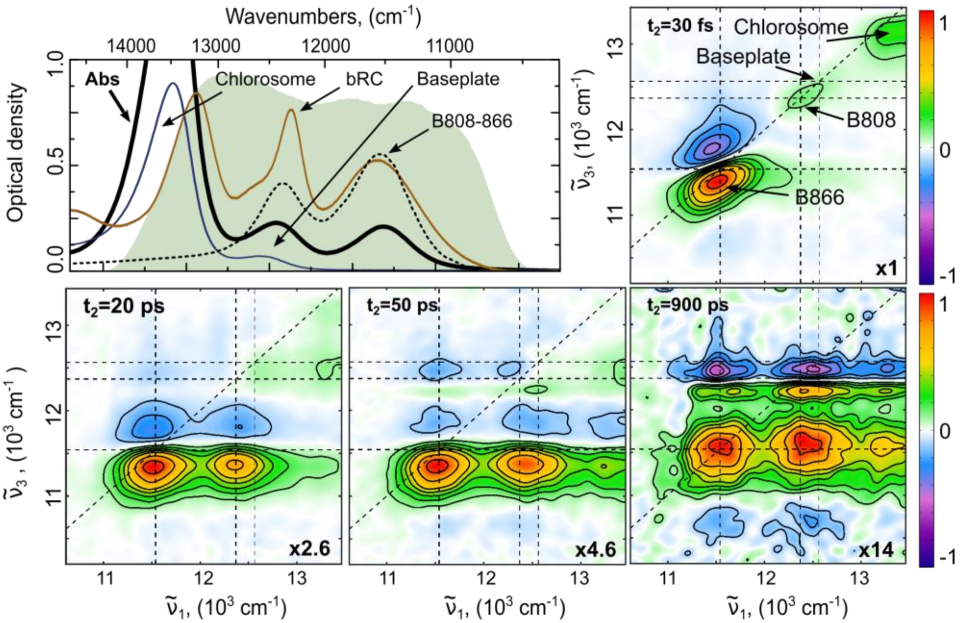

**Figure 20. Room temperature absorption and 2D spectra of *Cfx. aurantiacus* living cells**
Room temperature absorption spectrum of living *Cfx. aurantiacus* cells (solid black line) overlaid with the absorption spectra of isolated sub-units. All spectra were measured at room temperature by our group, except for the B808-866 complex, which was redrawn from [127]. The shaded area in the background presents the laser spectrum used for 2DES experiments. Four representative total absorptive 2D spectra of *Cfx. aurantiacus* living cells at room temperature are also shown. Each 2D spectrum was normalised to $t_2$=30 fs spectrum, as indicated in the lower right corner of the 2D spectra. Vertical/horizontal lines are set at 11540 cm$^{-1}$ (866 nm), 12370 cm$^{-1}$ (808 nm), and 12580 cm$^{-1}$ (795 nm). The figure was adapted from Paper V.

The 27 ps and 110 ps time components obtained from the global analysis of the B866 region corresponded to the excitation energy trapping in a charge-separated state in photo-active bRC.[50] This was clear from the diminishing of the signals from the B866 band and the rise of the band-shift signal in the reaction centres (see enhanced regions in two DAS in Fig. 21). It was concluded that the CT state forming was $P^+H_A^-$ since further ET to the primary quinone acceptor should take around 200 ps.[11] It was also suggested that two time constants for energy trapping originated from two types of B808-866 complexes in the cells. One was more efficiently coupled to the reaction centres, with ~28 ps time component for trapping, and the other was better connected to the baseplate.

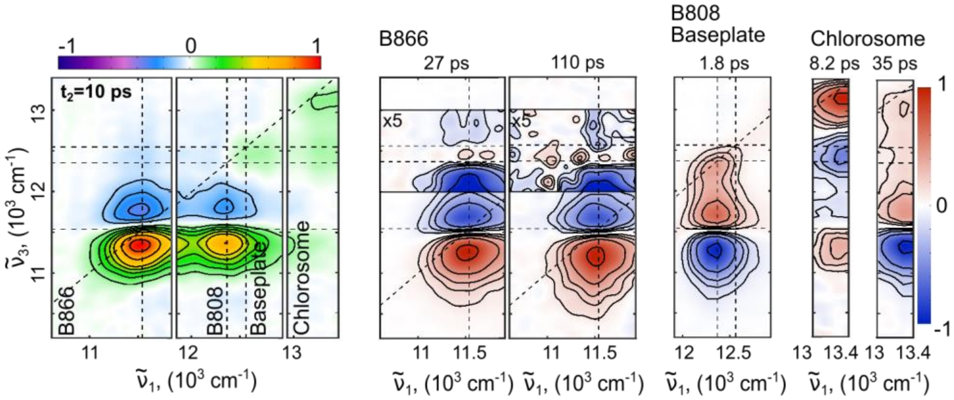

**Figure 21. Dissection of 2D spectra and the main DAS from the three regions**
Division of 2D spectra for the global analysis procedure and five main time components and their DAS. Characteristic times are presented above the spectra. Each DAS was normalised to one, and the band-shift regions of 27 ps and 110 ps DAS were additionally multiplied by 5 to make the weak signals visible. Figure adapted from Paper V.

Analysis from the B808 and the baseplate region indicated a rapid 1.8 ps EET between the B808→B866 bands.[49] The two DAS components from the global analysis of the chlorosome region correspond to the chlorosome to baseplate energy transfer in 8 ps[128] and baseplate to B808-866 EET in 35 ps[22]. Finally, the >1 ns DAS component (not presented), obtained in all three regions, indicated molecular relaxation to the ground state.

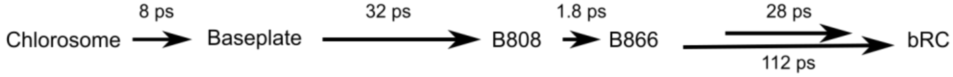

**Figure 22. EET and ET scheme via the whole photosynthetic unit**
Scheme and timescales of downhill excitation energy transfer (EET) and energy trapping inside the bacterial reaction centres (bRCs). Figure from Paper V.

The findings of Paper V were summarised in an energy transfer and trapping scheme, as in Fig. 22. A rapid energy transfer in the B808-866 complex fixed the energy in the B866 band and prevented the backward energy transfer. It was concluded that the EET bottlenecks in the PSU of *Cfx. aurantiacus* was between the baseplate and the core complex, yet also between the core complex and the bRC. This coincided with the spatial arrangement of photosynthetic complexes inside the unit, where the largest distances were expected between the baseplate and the B808 ring and also the B866 ring and the special pair in bRC.

# Concluding remarks

The main results of this thesis come from the three experimental sections: identifying vibronic coupling in Chl-type molecules, characterising excitation energy and electron transfer steps in two reaction centres ($bRC_{sph}$ and $bRC_{cfx}$), and probing energy transfer and trapping in the PSU of intact living cells of the green bacteria *Chloroflexus aurantiacus*. Experiments presented in this thesis also show the versatility and capabilities of two-dimensional electronic spectroscopy to track photo-induced processes in various systems, starting with single molecules and finishing with intact cells of photosynthetic bacteria.

The search for vibronic coupling in the Chl *c1* molecule (Paper I) aimed to identify the spectroscopic signatures of this phenomenon. Beating signals surviving suppressing polarisation sequence clearly indicated the presence of the vibronic coupling and provided an understanding of how the coupling potentially changed the states involved. Hopefully, with these spectroscopic signatures in mind, the vibronic coupling will be observed in many other Chl-type molecules (Chl *a*, BChl *a*, etc.).

The research on two different bacterial reaction centres ($bRC_{sph}$ and $bRC_{cfx}$, Papers II, III and IV) provided observations of initial CT states in the special pair dimers. Excellent temporal and spectral resolutions clearly illustrated the presence of this state and its involvement in the charge transfer process, yet also raised the question of its exact origin and the influence exerted by the protein environment of a special pair.

The room temperature 2DES experiments on living cells of the green bacteria *Chloroflexus aurantiacus* gave a close-to-physiology look at photo-induced processes in the intact PSUs. The study clarified the limiting transfer rates for the inner EET processes and how the overall high efficiency for energy transfer and charge separation is assured in these organisms.

# The outlook

I would like to start the outlook of the work presented in this thesis from the very beginning – its title. *Big lessons from small bacteria* immediately raises two questions: how big the photosynthetic bacteria are, and what can be learned from them? The answer about the size lies in the first chapter of this thesis. In contrast, the part about *big lessons* can cover a broad range of explanations and motivate studies of photosynthetic bacteria in the first place.

Efficiency and robustness are the two cornerstones of bacterial photosynthesis. If explored and understood, the knowledge of the exact mechanisms behind the photo-induced processes and their structure-function relationship to withstand harsh environments could become an essential part of future inventions. These might include improvements to using solar energy as a renewable source,[129–131] treatments and biomass generation in wastewater plants,[132–134] genetic modifications to develop varieties adapted to climate change or increasing crop yield through maximising photosynthesis,[135,136] to mention a few. Therefore, while the title of this work tends to summarise the immense potential of studying photosynthetic bacteria on its own, the subtitle concentrates on the key aspects of this thesis – following the primary steps of bacterial photosynthesis and learning more about its peculiarities using 2DES.

For the future, I hope that the findings and results of this work will encourage research and observations of precursor states to charge separation in other type II (and maybe type I) reaction centres. For this task, performing 2DES with attosecond pulses could help to catch the formation of the *minor* band-shift signals. The values of these minor shifts of accessory co-factors and the known structures of reaction centres are vital information needed to identify the exact origin of these initial states. In addition, it would be exciting to see many more 2DES experiments on intact cells of various photosynthetic bacteria and learn about their energy and electron transfer peculiarities. Performing these experiments close to the natural conditions for various bacteria (at higher/lower temperatures, different salinities and pH values) could help to find the connection between their extreme robustness and highly efficient photo-activity.

# References

1. Blankenship, R.E. Origin and early evolution of photosynthesis. *Photosynth. Res.*, **1992** 33 (2), 91–111.
2. Ort, D.R.; Yocum, C.F. Oxygenic Photosynthesis: The Light Reactions. (Ort DR, Yocum CF, Heichel IF. eds). Advances in Photosynthesis and Respiration. Springer Netherlands: Dordrecht; **1996**.
3. Blankenship, Robert E. Madigan, M.T.; Bauer, E.C. Anoxygenic Photosynthetic Bacteria. (Blankenship RE, Madigan MT, Bauer CE. eds). Advances in Photosynthesis and Respiration. Springer Netherlands: Dordrecht; **1995**.
4. Fleming, G.R.; Grondelle, R. Van. The Primary Steps of Photosynthesis. *Phys. Today*, **1994** 47 (2), 48–55.
5. Stirbet, A.; Lazár, D.; Guo, Y.; et al. Photosynthesis: basics, history and modelling. *Ann. Bot.*, **2020** 126 (4), 511–537.
6. Van Grondelle, R. Excitation energy transfer, trapping and annihilation in photosynthetic systems. *Biochim. Biophys. Acta - Rev. Bioenerg.*, **1985** 811 (2), 147–195.
7. Achenbach, L.A.; Carey, J.; Madigan, M.T. Photosynthetic and Phylogenetic Primers for Detection of Anoxygenic Phototrophs in Natural Environments. *Appl. Environ. Microbiol.*, **2001** 67 (7), 2922–2926.
8. Madigan, M.T.; Jung, D.O. An Overview of Purple Bacteria: Systematics, Physiology, and Habitats. **2009**; 1–15.
9. Castenholz, R.W.; Pierson, B.K. Ecology of Thermophilic Anoxygenic Phototrophs. In: Anoxygenic Photosynthetic Bacteria. (Blankenship RE, Madigan MT, Bauer CE. eds) Kluwer Academic Publishers: Dordrecht; **1995**; 87–103.
10. Borisov, A.Y.; Freiberg, A.; Godik, V.; et al. Kinetics of picosecond bacteriochlorophyll luminescence in vivo as a function of the reaction center state. *Biochim. Biophys. Acta - Bioenerg.*, **1985** 807 (3), 221–229.
11. Volk, M.; Scheidel, G.; Ogrodnik, A.; et al. High quantum yield of charge separation in reaction centers of Chloroflexus aurantiacus. *Biochim. Biophys. Acta - Bioenerg.*, **1991** 1058 (2), 217–224.
12. Pullerits, T.; Sundström, V. Photosynthetic Light-Harvesting Pigment−Protein Complexes: Toward Understanding How and Why. *Acc. Chem. Res.*, **1996** 29 (8), 381–389.
13. Sundström, V.; Pullerits, T.; Van Grondelle, R. Photosynthetic light-harvesting: Reconciling dynamics and structure of purple bacterial LH2 reveals function of photosynthetic unit. *J. Phys. Chem. B*, **1999** 103 (13), 2327–2346.

14. Cogdell, R.J.; Fyfe, P.K.; Barrett, S.J.; et al. The purple bacterial photosynthetic unit. *Photosynth. Res.*, **1996** 48 (1–2), 55–63.

15. Nielsen, J.T.; Kulminskaya, N. V.; Bjerring, M.; et al. In situ high-resolution structure of the baseplate antenna complex in Chlorobaculum tepidum. *Nat. Commun.*, **2016** 7 (1), 12454.

16. Staehelin, L.A.; Golecki, J.R.; Fuller, R.C.; et al. Visualization of the supramolecular architecture of chlorosomes (chlorobium type vesicles) in freeze-fractured cells of Chloroflexus aurantiacus. *Arch. Microbiol.*, **1978** 119 (3), 269–277.

17. Hu, X.; Ritz, T.; Damjanović, A.; et al. Photosynthetic apparatus of purple bacteria. *Q. Rev. Biophys.*, **2002** 35 (1), 1–62.

18. Saer, R.G.; Blankenship, R.E. Light harvesting in phototrophic bacteria: structure and function. *Biochem. J.*, **2017** 474 (13), 2107–2131.

19. Pšenčík, J.; Collins, A.M.; Liljeroos, L.; et al. Structure of Chlorosomes from the Green Filamentous Bacterium Chloroflexus aurantiacus. *J. Bacteriol.*, **2009** 191 (21), 6701–6708.

20. Blankenship, R.E. Molecular Mechanisms of Photosynthesis. Third. Wiley; **2002**.

21. Niedzwiedzki, D.M.; Blankenship, R.E. Singlet and triplet excited state properties of natural chlorophylls and bacteriochlorophylls. *Photosynth. Res.*, **2010** 106 (3), 227–238.

22. Müller, M.G.; Griebenow, K.; Holzwarth, A.R. Picosecond energy transfer and trapping kinetics in living cells of the green bacterium Chloroflexus aurantiacus. *Biochim. Biophys. Acta - Bioenerg.*, **1993** 1144 (2), 161–169.

23. Gouterman, M. Spectra of porphyrins. *J. Mol. Spectrosc.*, **1961** 6 (C), 138–163.

24. Oviedo, M.B.; Sánchez, C.G. Transition Dipole Moments of the $Q_y$ Band in Photosynthetic Pigments. *J. Phys. Chem. A*, **2011** 115 (44), 12280–12285.

25. Reimers, J.R.; Cai, Z.-L.; Kobayashi, R.; et al. Assignment of the Q-Bands of the Chlorophylls: Coherence Loss via $Q_x$−$Q_y$ Mixing. *Sci. Rep.*, **2013** 3 (1), 2761.

26. Womick, J.M.; Moran, A.M. Vibronic Enhancement of Exciton Sizes and Energy Transport in Photosynthetic Complexes. *J. Phys. Chem. B*, **2011** 115 (6), 1347–1356.

27. Tiwari, V.; Peters, W.K.; Jonas, D.M. Electronic resonance with anticorrelated pigment vibrations drives photosynthetic energy transfer outside the adiabatic framework. *Proc. Natl. Acad. Sci.*, **2013** 110 (4), 1203–1208.

28. Helfrich, M.; Bommer, B.; Oster, U.; et al. Chlorophylls of the c family: absolute configuration and inhibition of NADPH:protochlorophyllide oxidoreductase. *Biochim. Biophys. Acta - Bioenerg.*, **2003** 1605 (1–3), 97–103.

29. Sasaki, K.; Watanabe, M.; Suda, Y.; et al. Applications of photosynthetic bacteria for medical fields. *J. Biosci. Bioeng.*, **2005** 100 (5), 481–488.

30. Jungas, C. Supramolecular organization of the photosynthetic apparatus of Rhodobacter sphaeroides. *EMBO J.*, **1999** 18 (3), 534–542.

31. Pierson, B.K.; Castenholz, R.W. A phototrophic gliding filamentous bacterium of hot springs, Chloroflexus aurantiacus, gen. and sp. nov. *Arch. Microbiol.*, **1974** 100

(1), 5–24.

32. Kiley, P.J.; Kaplan, S. Molecular genetics of photosynthetic membrane biosynthesis in Rhodobacter sphaeroides. *Microbiol. Rev.*, **1988** 52 (1), 50–69.

33. Bahatyrova, S.; Frese, R.N.; Siebert, C.A.; et al. The native architecture of a photosynthetic membrane. *Nature*, **2004** 430 (7003), 1058–1062.

34. Şener, M.K.; Olsen, J.D.; Hunter, C.N.; et al. Atomic-level structural and functional model of a bacterial photosynthetic membrane vesicle. *Proc. Natl. Acad. Sci.*, **2007** 104 (40), 15723–15728.

35. Qian, P.; Swainsbury, D.J.K.; Croll, T.I.; et al. Cryo-EM Structure of the Rhodobacter sphaeroides Light-Harvesting 2 Complex at 2.1 Å. *Biochemistry*, **2021** 60 (44), 3302–3314.

36. Tani, K.; Nagashima, K.V.P.; Kanno, R.; et al. A previously unrecognized membrane protein in the Rhodobacter sphaeroides LH1-RC photocomplex. *Nat. Commun.*, **2021** 12 (1), 6300.

37. Timpmann, K.; Chenchiliyan, M.; Jalviste, E.; et al. Efficiency of light harvesting in a photosynthetic bacterium adapted to different levels of light. *Biochim. Biophys. Acta - Bioenerg.*, **2014** 1837 (10), 1835–1846.

38. Adams, P.G.; Hunter, C.N. Adaptation of intracytoplasmic membranes to altered light intensity in Rhodobacter sphaeroides. *Biochim. Biophys. Acta - Bioenerg.*, **2012** 1817 (9), 1616–1627.

39. Pullerits, T.; Hess, S.; Herek, J.L.; et al. Temperature Dependence of Excitation Transfer in LH2 of Rhodobacter sphaeroides. *J. Phys. Chem. B*, **1997** 101 (49), 10560–10567.

40. Nagarajan, V.; Parson, W.W. Excitation Energy Transfer between the B850 and B875 Antenna Complexes of Rhodobacter sphaeroides. *Biochemistry*, **1997** 36 (8), 2300–2306.

41. Pierson, B.K.; Castenholz, R.W. Studies of pigments and growth in Chloroflexus aurantiacus, a phototrophic filamentous bacterium. *Arch. Microbiol.*, **1974** 100 (1), 283–305.

42. Pierson, B.K.; Castenholz, R.W. Bacteriochlorophylls in gliding filamentous prokaryotes from hot springs. *Nat. New Biol.*, **1971** 233 (35), 25–27.

43. Tamiaki, H. Supramolecular structure in extramembraneous antennae of green photosynthetic bacteria. *Coord. Chem. Rev.*, **1996** 148, 183–197.

44. Olson, J.M. Chlorophyll Organization and Function in Green Photosynthetic Bacteria. *Photochem. Photobiol.*, **1998** 67 (1), 61–75.

45. Saga, Y.; Tamiaki, H. Transmission electron microscopic study on supramolecular nanostructures of bacteriochlorophyll self-aggregates in chlorosomes of green photosynthetic bacteria. *J. Biosci. Bioeng.*, **2006** 102 (2), 118–123.

46. Golecki, J.R.; Oelze, J. Quantitative relationship between bacteriochlorophyll content, cytoplasmic membrane structure and chlorosome size in Chloroflexus aurantiacus. *Arch. Microbiol.*, **1987** 148 (3), 236–241.

47. Bína, D.; Gardian, Z.; Vácha, F.; et al. Supramolecular organization of photosynthetic membrane proteins in the chlorosome-containing bacterium

Chloroflexus aurantiacus. *Photosynth. Res.*, **2014** 122 (1), 13–21.

48. Tang, K.; Urban, V.S.; Wen, J.; et al. SANS Investigation of the Photosynthetic Machinery of Chloroflexus aurantiacus. *Biophys. J.*, **2010** 99 (8), 2398–2407.
49. Novoderezhkin, V.I.; Taisova, A.S.; Fetisova, Z.G.; et al. Energy Transfers in the B808 – 866 Antenna from the Green Bacterium Chloroflexus aurantiacus. *Biophys. J.*, **1998** 74 (4), 2069–2075.
50. Causgrove, T.P.; Brune, D.C.; Wang, J.; et al. Energy transfer kinetics in whole cells and isolated chlorosomes of green photosynthetic bacteria. *Photosynth. Res.*, **1990** 26 (1), 39–48.
51. Van Dorssen, R.J.; Amesz, J. Pigment organization and energy transfer in the green photosynthetic bacterium Chloroflexus aurantiacus. III. Energy transfer in whole cells. *Photosynth. Res.*, **1988** 15 (2), 177–189.
52. Ermler, U.; Fritzsch, G.; Buchanan, S.K.; et al. Structure of the photosynthetic reaction centre from Rhodobacter sphaeroides at 2.65 Å resolution: cofactors and protein-cofactor interactions. *Structure*, **1994** 2 (10), 925–36.
53. Blankenship, R.E.; Feick, R.; Bruce, B.D.; et al. Primary photochemistry in the facultative green photosynthetic bacterium Chloroflexus aurantiacus. *J. Cell. Biochem.*, **1983** 22 (4), 251–261.
54. Pierson, B.K.; Thornber, J.P. Isolation and spectral characterization of photochemical reaction centers from the thermophilic green bacterium Chloroflexus aurantiacus strain J-10-f1. *Proc. Natl. Acad. Sci.*, **1983** 80 (1), 80–84.
55. Shuvalov, V.A.; Shkuropatov, A.Y.A.; Kulakova, S.M.; et al. Photoreactions of bacteriopheophytins and bacteriochlorophylls in reaction centers of Rhodopseudomonas sphaeroides and Chloroflexus aurantiacus. *Biochim. Biophys. Acta*, **1986** 849 (3), 337–346.
56. Scherer, P.O.J.; Fischer, S.F. Model studies to low-temperature optical transitions of photosynthetic reaction centers. II. Rhodobacter sphaeroides and Chloroflexus aurantiacus. *BBA - Bioenerg.*, **1987** 891 (2), 157–164.
57. Guo, Z.; Lin, S.; Xin, Y.; et al. Comparing the temperature dependence of photosynthetic electron transfer in chloroflexus aurantiacus and rhodobactor sphaeroides reaction centers. *J. Phys. Chem. B*, **2011** 115 (38), 11230-11238.
58. Feick, R.; Shiozawa, J.A.; Ertlmaier, A. Biochemical and Spectroscopic Properties of the Reaction Center of the Green Filamentous Bacterium, Chloroflexus Aurantiacus. In: Anoxygenic Photosynthetic Bacteria Kluwer Academic Publishers: Dordrecht; 699–708.
59. Ovchinnikov, Y.A.; Abdulaev, N.G.; Zolotarev, A.S.; et al. Photosynthetic reaction centre of Chloroflexus aurantiacus I. Primary structure of L-subunit. *FEBS Lett.*, **1988** 231 (1), 237–242.
60. Ovchinnikov, Y.A.; Abdulaev, N.G.; Shmuckler, B.E.; et al. Photosynthetic reaction centre of Chloroflexus aurantiacus Primary structure of M-subunit. *FEBS Lett.*, **1988** 232 (2), 364–368.
61. Parot, P.; Delmas, N. Structure of Chloroflexus aurantiacus reaction center: photoselection at low temperature. *Biochim. Biophys. Acta*, **1985** 809 , 137–140.

62. Hale, M.B.; Blankenship, R.E.; Fuller, R.C. Menaquinone is the sole quinone in the facultatively aerobic green photosynthetic bacterium Chloroflexus aurantiacus. *Biochim. Biophys. Acta - Bioenerg.*, **1983** 723 (3), 376–382.

63. Humphrey, W.; Dalke, A.; Schulten, K. VMD: Visual molecular dynamics. *J. Mol. Graph.*, **1996** 14 (1), 33–38.

64. Steffen, M.A.; Lao, K.; Boxer, S.G. Dielectric Asymmetry in the Photosynthetic Reaction Center. *Science,* **1994** 264 (5160), 810–816.

65. Stark, J. Beobachtungen über den Effekt des elektrischen Feldes auf Spektrallinien. I. Quereffekt. *Ann. Phys.*, **1914** 348 (7), 965–982.

66. Boxer, S.G. Stark Realities. *J. Phys. Chem. B,* **2009** 113 (10), 2972–2983.

67. Bublitz, G.U.; Boxer, S.G. Stark spectroscopy: applications in chemistry, biology, and materials science. *Annu. Rev. Phys. Chem.*, **1997** 48, 213–242.

68. Scherer, P.; Fischer, S. On the stark effect for bacterial photosynthetic reaction centers. *Chem. Phys. Lett.*, **1986** 131, 153–159.

69. Lockhart, D.J.; Boxer, S.G. Stark effect spectroscopy of Rhodobacter sphaeroides and Rhodopseudomonas viridis reaction centers. *Proc. Natl. Acad. Sci. U. S. A.*, **1988** 85 (1), 107–111.

70. Lin, S.; Taguchi, A.K.W.; Woodbury, N.W. Excitation Wavelength Dependence of Energy Transfer and Charge Separation in Reaction Centers from Rhodobacter sphaeroides : Evidence for Adiabatic Electron Transfer. *J. Phys. Chem.*, **1996** 100 (42), 17067–17078.

71. Breton, J.; Martin, J.L.; Fleming, G.R.; et al. Low-temperature femtosecond spectroscopy of the initial step of electron-transfer in reaction centers from photosynthetic purple bacteria. *Biochemistry*, **1988** 27 (21), 8276–8284.

72. Martin, J.L.; Breton, J.; Hoff, a J.; et al. Femtosecond spectroscopy of electron transfer in the reaction center of the photosynthetic bacterium Rhodopseudomonas sphaeroides R-26: Direct electron transfer from the dimeric bacteriochlorophyll primary donor to the bacteriopheophytin acceptor with a t. *Proc. Natl. Acad. Sci. USA*, **1986** 83 (4), 957–961.

73. van Brederode, M.E.; van Mourik, F.; van Stokkum, I.H.M.; et al. Multiple pathways for ultrafast transduction of light energy in the photosynthetic reaction center of Rhodobacter sphaeroides. *Proc. Natl. Acad. Sci.*, **1999** 96 (5), 2054–2059.

74. Fleming, G.R.; Martin, J.L.; Breton, J. Rates of primary electron transfer in photosynthetic reaction centres and their mechanistic implications. *Nature*, **1988** 333 (6169), 190–192.

75. Holzapfel, W.; Finkele, U.; Kaiser, W.; et al. Initial electron-transfer in the reaction center from Rhodobacter sphaeroides. *Proc. Natl. Acad. Sci. U. S. A.*, **1990** 87 (13), 5168–5172.

76. Ziolek, M.; Pawlowicz, N.; Naskrecki, R.; et al. Electron transfer in the reaction center of the Rb. sphaeroides R-26 studied by transient absorption. *J. Phys. Chem. B*, **2005** 109 (38), 18171–18176.

77. Becker, M.; Nagarajan, V.; Middendorf, D.; et al. Temperature dependence of the initial electron-transfer kinetics in photosynthetic reaction centers of Chloroflexus

aurantiacus. *BBA - Bioenerg.*, **1991** 1057 (3), 299–312.

78. Kirmaier, C.; Blankenship, R.E.; Holten, D. Formation and decay of radical-pair state $P^+I^-$ in Chloroflexus aurantiacus reaction centers. *BBA - Bioenerg.*, **1986** 850 (2), 275–285.

79. Vermeglio, A.; Paillotin, G. Structure of Rhodopseudomonas viridis reaction centers. Absorption and photoselection at low temperature. *Biochim. Biophys. Acta*, **1982** 681 (1), 32–40.

80. Huber, H.; Meyer, M.; Scheer, H.; et al. Temperature dependence of the primary electron transfer reaction in pigment-modified bacterial reaction centers. *Photosynth. Res.*, **1998** 55 (2–3), 153–162.

81. Klevanik, A. V.; Ganago, A.O.; Shkuropatov, A.Y.A.; et al. Electron-phonon and vibronic structure of absorption spectra of the primary electron donor in reaction centers of Rhodopseudomonas viridis, Rhodobacter sphaeroides and Chloroflexus aurantiacus at 1.7-70 K. *FEBS Lett.*, **1988** 237 (1), 61–64.

82. Hoff, A.J.; den Blanken, H.J.; Vasmel, H.; et al. Linear-dichroic triplet-minus-singlet absorbance difference spectra of reaction centers of the photosynthetic bacteria Chromatium vinosum, Rhodopseudomonas sphaeroides R-26 and Rhodospirillum rubrum S1. *Biochim. Biophys. Acta*, **1985** 806 (3), 389–397.

83. Huang, L.; Ponomarenko, N.; Wiederrecht, G.P.; et al. Cofactor-specific photochemical function resolved by ultrafast spectroscopy in photosynthetic reaction center crystals. *Proc. Natl. Acad. Sci. U.S.A.*, **2012** 109 (13), 4851–4856.

84. Hoff, A.J. Bacterial Reaction Centers Are Intrinsically Heterogeneous. In: The Photosynthetic Bacterial Reaction Center: Structure and Dynamics. (Breton J, André V. eds) Plenum Press: New York; **1988**; 89–101.

85. Niedringhaus, A.; Policht, V.R.; Sechrist, R.; et al. Primary processes in the bacterial reaction center probed by two-dimensional electronic spectroscopy. *Proc. Natl. Acad. Sci.*, **2018** 115 (14), 3563–3568.

86. Feick, R.; Martin, J.L.; Breton, J.; et al. Biexponential Charge Seapration and Monoexponential Decay of $P^+H^−$ in Reaction Centers of Chloroflexus Aurantiacus. In: Reaction Centers of Photosynthetic Bacteria. (M.-E. Michel-Beyerle. ed) Springer-Verlag: Berlin; **1990**; 181–188.

87. Cho, M. Coherent Two-Dimensional Optical Spectroscopy. *Chem. Rev.*, **2008** 108 (4), 1331–1418.

88. Hamm, P.; Zanni, M. Concepts and Methods of 2D Infrared Spectroscopy. Cambridge University Press, **2011**.

89. Mukamel, S. Principles of Nonlinear Optics and Spectroscopy. New York: Oxford University Press, **1995**.

90. Abramavicius, D.; Palmieri, B.; Voronine, D. V.; et al. Coherent Multidimensional Optical Spectroscopy of Excitons in Molecular Aggregates; Quasiparticle versus Supermolecule Perspectives. *Chem. Rev.*, **2009** 109 (6), 2350–2408.

91. Gelzinis, A.; Augulis, R.; Butkus, V.; et al. Two-dimensional spectroscopy for non-specialists. *Biochim. Biophys. Acta - Bioenerg.*, **2019** 1860 (4), 271–285.

92. Jonas, D.M. Two-Dimensional Femtosecond Spectroscopy. *Annu. Rev. Phys.*

*Chem.*, **2003** 54 (1), 425–463.

93. Tollerud, J.O.; Davis, J.A. Coherent multi-dimensional spectroscopy: Experimental considerations, direct comparisons and new capabilities. *Prog. Quantum Electron.*, **2017** 55, 1–34.

94. Fuller, F.D.; Ogilvie, J.P. Experimental Implementations of Two-Dimensional Fourier Transform Electronic Spectroscopy. *Annu. Rev. Phys. Chem.*, **2015** 66 (1), 667–690.

95. Hybl, J.D.; Albrecht, A.W.; Gallagher Faeder, S.M.; et al. Two-dimensional electronic spectroscopy. *Chem. Phys. Lett.*, **1998** 297 (3–4), 307–313.

96. Butkus, V.; Zigmantas, D.; Abramavicius, D.; et al. Distinctive character of electronic and vibrational coherences in disordered molecular aggregates. *Chem. Phys. Lett.*, **2013** 587, 93–98.

97. Butkus, V.; Zigmantas, D.; Valkunas, L.; et al. Vibrational vs. electronic coherences in 2D spectrum of molecular systems. *Chem. Phys. Lett.*, **2012** 545, 40–43.

98. Thyrhaug, E.; Schröter, M.; Bukartė, E.; et al. Intraband dynamics and exciton trapping in the LH2 complex of Rhodopseudomonas acidophila. *J. Chem. Phys.*, **2021** 154 (4), 045102.

99. Dostál, J.; Mančal, T.; Augulis, R.; et al. Two-Dimensional Electronic Spectroscopy Reveals Ultrafast Energy Diffusion in Chlorosomes. *J. Am. Chem. Soc.*, **2012** 134 (28), 11611–11617.

100. Šanda, F.; Perlík, V.; Lincoln, C.N.; et al. Center Line Slope Analysis in Two-Dimensional Electronic Spectroscopy. *J. Phys. Chem. A*, **2015** 119 (44), 10893–10909.

101. Yang, M.; Fleming, G.R. Third-order nonlinear optical response of energy transfer systems. *J. Chem. Phys.*, **1999** 111 (1), 27–39.

102. Malý, P.; Mančal, T. Signatures of Exciton Delocalization and Exciton–Exciton Annihilation in Fluorescence-Detected Two-Dimensional Coherent Spectroscopy. *J. Phys. Chem. Lett.*, **2018** 9 (19), 5654–5659.

103. Butkus, V.; Alster, J.; Bašinskaitė, E.; et al. Discrimination of Diverse Coherences Allows Identification of Electronic Transitions of a Molecular Nanoring. *J. Phys. Chem. Lett.*, **2017** 8 (10), 2344–2349.

104. Thyrhaug, E.; Tempelaar, R.; Alcocer, M.J.P.; et al. Identification and characterization of diverse coherences in the Fenna–Matthews–Olson complex. *Nat. Chem.*, **2018** 10 (7), 780–786.

105. Mančal, T.; Dostál, J.; Pšenčík, J.; et al. Transfer of vibrational coherence through incoherent energy transfer process in Förster limit. *Can. J. Chem.*, **2014** 92 (2), 135–143.

106. Augulis, R.; Zigmantas, D. Two-dimensional electronic spectroscopy with double modulation lock-in detection: enhancement of sensitivity and noise resistance. *Opt. Express*, **2011** 19 (14), 13126–13133.

107. Augulis, R.; Zigmantas, D. Detector and dispersive delay calibration issues in broadband 2D electronic spectroscopy. *J. Opt. Soc. Am. B*, **2013** 30 (6), 1770.

108. Singh, V.P.; Westberg, M.; Wang, C.; et al. Towards quantification of vibronic

coupling in photosynthetic antenna complexes. *J. Chem. Phys.*, **2015** 142, 212446.

109. Paleček, D.; Edlund, P.; Westenhoff, S.; et al. Quantum coherence as a witness of vibronically hot energy transfer in bacterial reaction center. *Sci. Adv.*, **2017** 3 (9).

110. Alster, J.; Lokstein, H.; Dostál, J.; et al. 2D spectroscopy study of water-soluble chlorophyll-binding protein from Lepidium virginicum. *J. Phys. Chem. B,* **2014** 118 (13), 3524–3531.

111. Van Stokkum, I.H.M.; Larsen, D.S.; Van Grondelle, R. Global and target analysis of time-resolved spectra. *Biochim. Biophys. Acta*, **2004** 1657 (2), 82–104.

112. Büchel, C. Light harvesting complexes in chlorophyll c-containing algae. *Biochim. Biophys. Acta - Bioenerg.*, **2020** 1861 (4), 148027.

113. Shi, Y.; Liu, J.Y.; Han, K.L. Investigation of the internal conversion time of the chlorophyll a from S3, S2 to S1. *Chem. Phys. Lett.*, **2005** 410, 260–263.

114. Visser, H.M.; Somsen, O.J.; van Mourik, F.; et al. Direct observation of sub-picosecond equilibration of excitation energy in the light-harvesting antenna of Rhodospirillum rubrum. *Biophys. J.*, **1995** 69, 1083–1099.

115. Tomar, V. Raman Spectroscopy of Algae: A Review. *J. Nanomed. Nanotechnol.*, **2012** 03 (02), 1000131.

116. Arnett, D.C.; Moser, C.C.; Dutton, P.L.; et al. The first events in photosynthesis: Electronic coupling and energy transfer dynamics in the photosynthetic reaction center from Rhodobacter sphaeroides. *J. Phys. Chem. B*, **1999** 103 (11), 2014–2032.

117. Paleček, D.; Edlund, P.; Gustavsson, E.; et al. Potential pitfalls of the early-time dynamics in two-dimensional electronic spectroscopy. *J. Chem. Phys.*, **2019** 151 (2), 024201.

118. Schweitzer, G.; Hucke, M.; Griebenow, K.; et al. Charge separation kinetics in isolated photosynthetic reaction centers of Chloroflexus aurantiacus (with $Q_A$ reduced) at low temperatures. *Chem. Phys. Lett.*, **1992** 190 (1–2), 149–154.

119. Yakovlev, A.G.; Shuvalov, V.A. Coherent intradimer dynamics in reaction centers of photosynthetic green bacterium Chloroflexus aurantiacus. *Sci. Rep.*, **2020** 10 (1), 228.

120. Renger, T. Theory of optical spectra involving charge transfer states: Dynamic localization predicts a temperature dependent optical band shift. *Phys. Rev. Lett.*, **2004** 93 (18), 1–4.

121. Zazubovich, V.; Matsuzaki, S.; Johnson, T.W.; et al. Red antenna states of photosystem I from cyanobacterium Synechococcus elongatus: a spectral hole burning study. *Chem. Phys.*, **2002** 275 (47), 47–59.

122. Lösche, M.; Feher, G.; Okamura, M.Y. The Stark effect in reaction centers from Rhodobacter sphaeroides R-26 and Rhodopseudomonas viridis. *Proc. Natl. Acad. Sci. U.S.A*, **1987** 84 (21), 7537–7541.

123. Mančal, T.; Valkunas, L.; Fleming, G.R. Theory of exciton-charge transfer state coupled systems. *Chem. Phys. Lett.*, **2006** 432 (1–3), 301–305.

124. Artz, K.; Williams, J.C.; Allen, J.P.; et al. Relationship between the oxidation potential and electron spin density of the primary electron donor in reaction centers from Rhodobacter sphaeroides. *Proc. Natl. Acad. Sci. U. S. A.*, **1997** 94 (25), 13582–

13587.

125. Lendzian, F.; Huber, M.; Isaacson, R.A.; et al. The electronic structure of the primary donor cation radical in Rhodobacter sphaeroides R-26: ENDOR and TRIPLE resonance studies in single crystals of reaction centers. *Biochim. Biophys. Acta - Bioenerg.*, **1993** 1183 (1), 139–160.

126. Cohen Stuart, T.A.; van Grondelle, R. Multipulse spectroscopy on the wild-type and YM210W Bacterial Reaction Centre uncovers a new intermediate state in the special pair excited state. *Chem. Phys. Lett.*, **2009** 474 (4-6), 352–356.

127. Xin, Y.; Lin, S.; Montaño, G.A.; et al. Purification and Characterization of the B808–866 Light-harvesting Complex from Green Filamentous Bacterium Chloroflexus aurantiacus. *Photosynth. Res.*, **2005** 86 (1–2), 155–163.

128. Savikhin, S.; Zhu, Y.; Lin, S.; et al. Femtosecond spectroscopy of chlorosome antennas from the green photosynthetic bacterium chloroflexus aurantiacus. *J. Phys. Chem.*, **1994** 98 (40), 10322–10334.

129. McConnell, I.; Li, G.; Brudvig, G.W. Energy conversion in natural and artificial photosynthesis. *Chem. Biol.*, **2010** 17 (5), 434–447.

130. Cogdell, R.J.; Brotosudarmo, T.H.P.; Gardiner, A.T.; et al. Artificial photosynthesis - Solar fuels: Current status and future prospects. *Biofuels*, **2010** 1 (6), 861–876.

131. Benniston, A.C.; Harriman, A. Artificial photosynthesis. *Mater. Today*, **2008** 11 (12), 26–34.

132. Okubo, Y.; Futamata, H.; Hiraishi, A. Characterization of phototrophic purple nonsulfur bacteria forming colored microbial mats in a swine wastewater ditch. *Appl. Environ. Microbiol.*, **2006** 72 (9), 6225–6233.

133. Alloul, A.; Cerruti, M.; Adamczyk, D.; et al. Operational strategies to selectively produce purple bacteria for microbial protein in raceway reactors. *Environ. Sci. Technol.*, **2021** 55 (12), 8278–8286.

134. Lowrey, J.; Brooks, M.S.; McGinn, P.J. Heterotrophic and mixotrophic cultivation of microalgae for biodiesel production in agricultural wastewaters and associated challenges—a critical review. *J. Appl. Phycol.*, **2015** 27 (4), 1485–1498.

135. Simkin, A.J.; Faralli, M.; Ramamoorthy, S.; et al. Photosynthesis in non-foliar tissues: implications for yield. *Plant J.*, **2020** 101 (4), 1001–1015.

136. Manjarrez-Sanchez, J.; Martinez-Carrillo, G. Dataset of photosynthesis and photosynthetic factors measurements of greenhouse tomato. *Data Br.*, **2020** 32, 106274.

LUND
UNIVERSITY

Faculty of Science
Department of Chemistry
Division of Chemical Physics

ISBN 978-91-7422-932-5

Printed by Media-Tryck, Lund 2023 NORDIC SWAN ECOLABEL 3041 0903